The viability of CL subgrain imaging for determining paleostresses in quartz

Master thesis, Earth Structure and Dynamics

R. J. Jansen (4104560)

Department of Earth Sciences, Faculty of Geosciences,

Utrecht University

Abstract

The field of paleopiezometry has long been an important tool in the determination of paleo stresses. In order to make an as accurately as possible stress estimate, it is necessary that the microstructures used for paleopiezometry are measured as accurately as possible. This thesis aims to determine if cathodoluminescence (CL) imaging is a viable alternative or addition to light microscopy and/or electron backscatter diffraction (EBSD), with regards to subgrain detection and measurement. To achieve this aim, four different detection methods are each applied to four samples. These four methods are light microscopy, scanning electron microscopy with CL detector (SEM-CL), electron microprobe mapping and EBSD mapping. Three of the studied samples are naturally deformed and one experimentally. To determine the accuracy of the subgrain detection methods, stress estimates are made using paleopiezometry. These stress estimates are then compared to stress estimates made from recrystallized grain paleopiezometry of the same samples. The observations and data that results from this thesis indicates that while CL is a useful and fast method for detecting subgrains, it cannot be used without a second method to distinguish between subgrain boundaries and other microstructures i.e. Dauphiné twins.

Introduction

Quartz is one of the main components of the earth's crust and therefore its properties are important to crustal deformation *(Wedepohl, 1995; Rudnick and Gao, 2003)*. The study of different kinds of microstructures present in quartz can be a useful tool in determining the deformation mechanisms and paleostress in quartz. Out of the different microstructures present in quartz, the focus of this thesis will lay on subgrains and Dauphiné twinning, which can be used as paleo-stress indicators *(Twiss, 1977; White 1979; Stipp and Tullis, 2003;)*.

Various techniques have been used to detect and study the different deformation microstructures in quartz, each with their own advantages and disadvantages. The most basic of these techniques is light microscopy, which has as severe limitation that it only reliably depicts high angle misorientations (>10^{o}) and does not always pick up lower angle misorientations and twinning *(Spry et al., 1969; Trimby and Prior, 1999)*.

Electron backscatter diffraction (EBSD) can detect and distinguish between grain boundaries, subgrain boundaries and Dauphiné twins (*Prior et al. 1996; Neumann, 2000; Lloyd, 2000)*. Conventional EBSD can only measure misorientation angles down to ~0.5-0.3^{o}. However, high-angular resolution

electron backscatter diffraction data (HR-EBSD) has a lower detection limit of ~0.01° *(Goddard et al., T.B.D.; Wallis et al., 2019).* This HR-EBSD however, takes significantly longer to execute than conventional EBSD and it is used on single grains, not for larger area maps, making it unsuitable for the larger area maps that are needed for (sub)grain size analysis.

Unlike light microscopy and EBSD mapping, cathodoluminescence (CL) imaging is effective for imaging defects in the crystal structure that result from impurities *(Götze et al., 1999, 2001.; Götze, 2009;)* as well as high and low angle misorientation boundaries and other deformation microstructures. *(Hamers et al., 2016).* These deformation microstructures are most distinct in a red filtered CL image under a SEM-CL microscope *(Hamers et al., 2016)*. CL imaging does not distinguish between grain boundaries, subgrain boundaries and Dauphiné twins. SEM-CL imaging is also significantly faster than EBSD mapping.

The aim of this research is to determine if CL imaging is a viable alternative or addition to light microscopy and EBSD, with regards to stress estimation from subgrain sizes. This comparison is made in two different ways. The first method of comparison is a visual comparison between the different techniques to identify which method can detect the largest amount of subgrain boundaries and Dauphiné twins, and which method can distinguish between the two. The second method is comparing the resulting subgrain sizes, and thus stress estimates, to the stress estimates that were calculated using the recrystallized grain sizes obtained from light microscopy. In doing this it will be assumed that the stress estimates resulting from the recrystallized grain sizes are the most accurate. By comparing the subgrain size stress estimates from the different techniques to this recrystallized grain size stress estimate, more insight will be gained into which method for subgrain detection, and thus stress estimation, is the better option.

Materials and methods

Samples

Four samples were studied, three of which were naturally deformed samples taken from Cap de Creus in north-eastern Spain, while the fourth sample was experimentally deformed in a lab by Michael Stipp (*Stipp and Tullis, 2003)*. The three Cap de Creus quartzites were sampled from three different locations. CC98-4 and CC98-4c were both taken from the same shear zone, with CC98-4 taken from inside the shear zone, and CC98-4c taken from outside the same shear zone. The sample Cml-2 was taken from a pegmatite rich area and may have contained beta-quartz indicating it has experienced temperatures higher than 573 ^{o}C. The 1024 sample obtained from Michael Stipp has made the transition to β-quartz and back, and has been deformed at 1000 ^{o}C and a strain-rate of 1.8-2.3*10^{-6} s^{-1} (*Stipp and Tullis, 2003)*.

The three naturally deformed Cap de Creus samples were polished following the same method as described in *Hamers et al., 2016*. The samples were polished with Al_2O_3 to a 0.3µm finish, finishing by 20 minutes of colloidal silica (Syton) chemical mechanical polishing. After polishing, a thin layer of carbon coating was used to coat the samples, which reduces charging and drift problems. These processes make the samples of high enough quality for EBSD mapping. For the sample preparation of sample 1024 see Gleason and Tullis (1995).

For the light microscopy a Zeiss Axio Scope.A1 microscope was used with the magnifications used ranging from 2.5 to 40 times.

For all images and maps obtained during this research, recrystallized and subgrain boundary estimates have been made by hand using the linear intersect method *(Smith and Guttman, 1953; Pickering, 1976)*.

SEM-CL

The SEM-CL images were recorded in a FEI Nova Nanolab 600 dual beam SEM with a panchromatic Gatan PanaCL detector with a detection range of 185-850nm (Gatan UK, Oxford, UK), with red (595-850nm), green (495-575nm) and blue (185-510nm) colour filters. The images were made at room temperature, with an electron acceleration voltage of 10kV, electron beam currents of 6.4nA and a dwell time of 30µs. To create clearer images, the same area was scanned 2 or 3 times under these settings in some cases. This process increased the contrast between the brighter lines and the grey background.

To create a composite RGB image from these three colour filtered images, Adobe Photoshop was used.

This was done by adding each of the three colour filtered images to their respective blue, green and red channels and so combining them together into a full RGB (false colour) image. Because the contrast and brightness of the images have been adjusted, to make the contrast between the different features inside the images as clear as possible, the images do not indicate the precise and specific CL emission wavelength, but instead indicate what the dominant colour range is of the different features in the sample.

Electron-Microprobe

Hyperspectral CL maps were made in a JEOL JXA-8530F Hyperprobe field emission electron probe micro analyser with a xCLent IV CL spectrometry system. This system has a wavelength detection range of 200-900nm covering almost the same spectrum as the SEM-CL. Unlike the SEM-CL imaging, the microprobe collects the complete spectrum for each point in the map, after which the user defines what wavelengths are used to make each image. All samples maps were made with an accelerating voltage of 10kV and a beam current of 40.1nA. the only exception to this was the map sample CML-2 which was made with an accelerating voltage of 15kV. All maps were made with a dwell time of 40ms and a step size of 0.30µm.

EBSD

To detect twinning and subgrains and to make the distinction between these two, EBSD maps were recorded from the same area as the SEM-CL images. The EBSD maps were made using a Philips XL30 SFEG SEM equipped with a Nordlys camera and Oxford-HKL Aztec software. For the three naturally deformed samples an electron voltage of 20kV was used, with a nominal electron beam current of ~2.4nA and an aperture of 50µm. For the experimentally deformed sample an electron voltage of 30kV was used with a nominal electron beam current of ~2.4nA and a aperture of 50µm. The step size for the three naturally deformed samples is 2.5µm while the step size for the experimentally deformed sample is 1µm. This difference was chosen because the experimentally deformed sample showed smaller subgrains in the SEM-CL segment of this research. For all samples the working distance was ~20mm and the sample tilt was ~70^{o}. The collection rates lay at ~1ms for the naturally deformed samples and at ~2.5ms for the experimentally deformed sample. Indexing rates are above 96% except for sample CC98-4c where the index rate is ~94%.

EBSD data were processed using HKL Channel 5 software, in which standard iterative noise reduction and wild spike removal were applied to all images. This is done starting from iterative noise reduction using 8 neighbours all the way down until 5 neighbours. This is the lowest number of neighbours that has been used during noise reduction. In some cases after this standard noise reduction the decision was made to apply a Kuwahara filter to the data *(Brough et al,. 2006)*. This was done to clean the image up even more and make the grain boundaries more clear and continuous. The Kuwahara filter was applied with a 3x3 matrix, a smoothing angle of 5^{o} and an artefact filter of 1^{o}.

To construct the grain boundary maps from the EBSD data, boundaries had to be set for which misorientation angles would be depicted in which colours. For the purpose of this research, four categories were decided on. Misorientations of 60^{o} with a maximum deviation angle of 5^{o} on the (0001) axis are depicted in red and considered to be Dauphiné twins. Every other misorientation larger than 10^{o} is considered to be a recrystallized grain-boundary or normal grain boundary (*Goddard et al., T.B.D.)* and is depicted by the black lines. Every misorientation below 10^{o} is considered to be a subgrain boundary. However, the choice was made to further distinguish between normal subgrain boundaries, with a misorientation angle between 2^{o} and 10^{o}, depicted in yellow, and subgrain boundaries with a lower angular misorientation than 2^{o}, depicted in green. The lower angular misorientation boundary of these green lines can vary between 1^{o} and 0.3^{o}. What the lower boundary of these green lines is will be annotated at every image in this thesis to avoid confusion. This distinction between the yellow and green lines is made to clarify where the boundaries are located that are more difficult to detect using EBSD, and to better see what influence the lowering of the angular misorientation detection limit has on the resulting EBSD grain-boundary maps.

Results

Light microscopy

In light microscopy it can be difficult to accurately make a distinction between recrystallized grains and subgrains. This distinction however, can be made with EBSD mapping which is done later in this thesis. However, to avoid confusion these microstructures are already identified by their proper name in this section of the thesis. Light microscopy is the most basic method for analysing the different samples that are used in this thesis. Subgrain boundaries are defined as having a misorientation angle lower than 15-10^{o} (*Goddard et al., T.B.D.).* For this thesis the decision was made to set the boundary between subgrain boundaries and other grain boundaries at 10^{o}. As stated before, since light microscopy can only reliably pick up misorientations that are larger than 10^{o}, it would be expected that the subgrains are poorly visible in a light microscopy image.

Figure 1a depicts a light microscopy image from roughly the same area as the SEM-CL image in figure 1b. the red arrow indicates the same fracture in both images as a reference. The light microscopy image does depict some of what appear to be subgrains around the edges of the larger grains, these are however few and far between. The SEM-CL image in figure 1 b, most predominantly the larger grain that has been circled in red on both images, depicts significantly more structures and possible subgrains than the light microscopy image does. The subgrains that do show up inside the light microscopy image are much larger than those that can be detected in the SEM-CL image. This is because the light microscopy does not pick up the small angular misorientations between different subgrains and thus are grouped together with a single extinction angle where the small difference are not noticeable, or it will look like a gradual extinction across a larger grain.

Recrystallized grains are depicted in the light microscopy image as well as in the SEM-CL image (blue circle). However, when comparing the two images, the recrystallized grains are larger in the light microscopy image than in the SEM-CL image. This is because the SEM-CL image picks up more recrystallized grains and can better distinguish between them.

These observed detection differences between light microscopy and SEM-CL imaging are consistent across all four samples. In all cases the subgrains that are detected in a SEM-CL image are more numerous and smaller than in a light microscopy image taken from roughly the same area. The comparison images of the other three samples, CC98-4, CC98-4c and CML-2, can be found in appendices 1a-d.

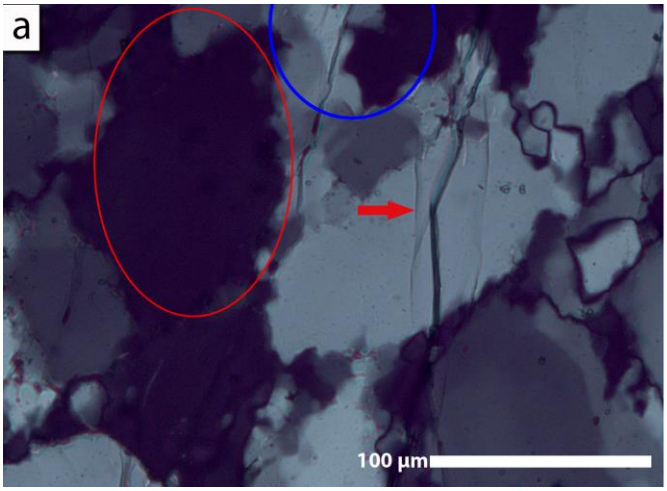

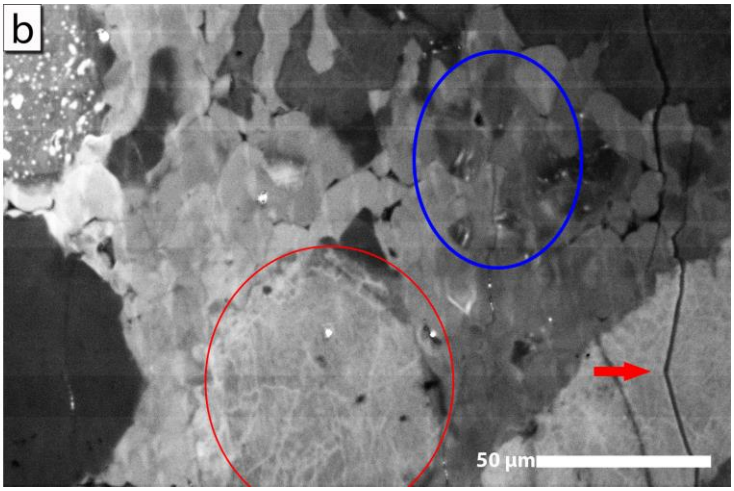

Figure.1 Figure 1a shows a light microscopy image of sample 1024. The image was taken at a 20 times magnification. The imaged depicts some subgrains located mostly around the edge of the larger grains. the medium sized grains located between the larger grains are recrystallized grains. Figure 1b shows a blue filtered SEM-CL image of roughly the same location as figure 1a and is slightly rotated counter clockwise compared to figure 1a. Figure 1b shows the same recrystallized grains between the larger grains (blue circle). However, in this figure they are smaller than in figure 1a. The red arrow in both image a and b indicate the same crack. And the red circle in both images, surround the same grain. The SEM-CL shows a lot of possible subgrains inside the red circled grain. The same grain shows almost no subgrains in the light microscopy image.

SEM-CL

In SEM-CL it is impossible to make the distinction between which of the bright lines are subgrain boundaries and which are twins. The EBSD section further on in the results shows which of these lines are which. Until a clear distinction between subgrain boundaries and twins can be made in the EBSD section of this thesis, all the bright lines will be referred to as subgrain boundary since they are the feature that predominantly occurs in these samples.

For the three Cap de Creus quartzites only a red filtered CL filter was used, as the subgrain boundaries predominantly emit a higher red CL signal than the grains they are located in *(Hamers et al., 2016)*. Repeated scanning of the same area shows that this longer exposure of the sample results into a clearer distinction between the subgrain boundaries and the surrounding grain as shown in figure 2. In figure 2 the left image is a SEM-CL red filtered image of a small part of sample CML-2. The right image shows the same location only after a second scan was made directly after the first one. The second scan makes the subgrain boundaries and other structures present more clearly defined.

To make the distinction between the subgrain boundaries and the surrounding grains even more clear post processing has been applied to the SEM-CL images. In this post processing the only variables that have been altered are the brightness of the image and the contrast of the image. An example of this is shown in figure 3.

Not all the bright lines on a red filtered SEM-CL image are subgrain boundaries. For a line to be considered a possible subgrain boundary it needs to be continuous. Therefore the lines indicated in figure 3 by arrows 1 and 2 cannot be subgrains. The type of short lines indicated by arrow 1 are most likely a group of clustered dislocations that have not formed into subgrain boundaries or recrystallized grain boundaries. The type of lines indicated by arrow 2 are most likely the result of surface damage that occurred during polishing of the thin section. The red arrows again indicate possible subgrain boundaries or Dauphiné twins. No clear method to distinguish between the Dauphiné twins and subgrain boundaries with a SEM-CL image has been found, as the SEM-CL image measures no relative orientation angles between the different subgrains like for example EBSD does. There also does not seem to be a clear brightness difference between the different lines that could be used as a way to distinguish between subgrain boundaries and Dauphiné twins.

The experimentally deformed sample 1024, obtained from Michael Stipp, gave a different result than seen in the Cap de Creus samples, and Hamers et al. (2016). Unlike the Cap de Creus quartzites this sample shows the subgrain boundaries more clearly

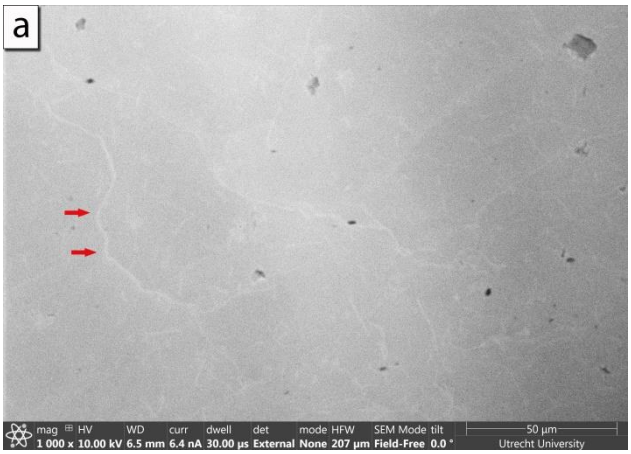

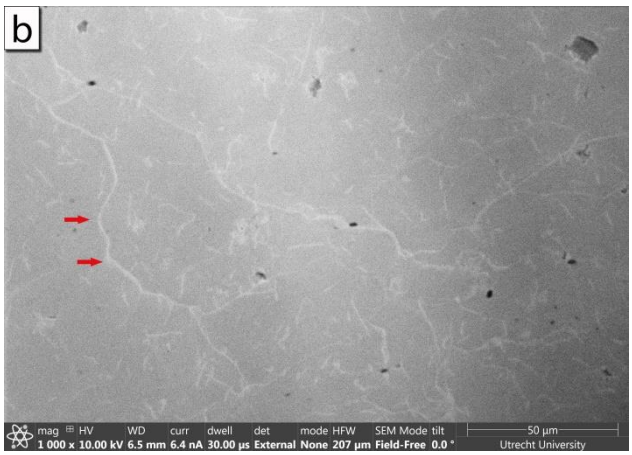

Figure.2 SEM-CL red filtered image of a small part of sample CML-2. Figure 2a depicts the scanned area after the first scan. The subgrain boundaries and other structures can be seen to be slightly lighter than the surrounding grains. A clear subgrain boundary is indicated by the red arrows. Figure 2b depicts a SEM-CL red filtered image of the same location as in figure 2a. This second scan was taken directly after the first scan that produced the image in 2a. The distinction between the subgrain boundaries and the surrounding grains is more defined in this image. The same subgrain boundary is again indicated by the red arrows.

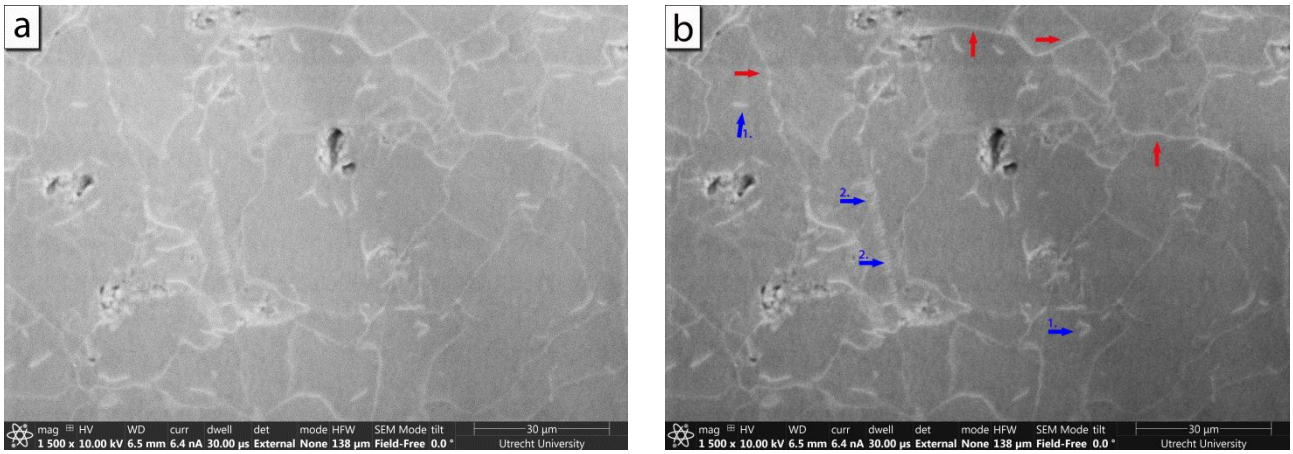

Figure.3 SEM-CL red filtered image of a small part of sample CC98-4. Figure 3a depicts the unaltered image as taken from the SEM-CL. Figure 3b depicts the same image only post processed in Photoshop to up the contrast and lower the overall brightness of the image. This is done to increase the contrast between the dislocation structures, including subgrain boundaries, and the surrounding grains. The blue arrows with a 1 next to the arrow show small lines that cannot be clearly defined as a specific microstructure and thus won't be counted when determining subgrain size. The blue arrows with a 2 next to the arrow indicate surface damage. This type of damage occurs all throughout the samples and is thought to be the result of polishing. The red arrows again show examples of possible subgrain boundaries. The dark grey/black spots in the sample are either holes in the sample/micro-fractures or dirt on the surface of the sample that hasn't fully been cleaned off during sample preparation.

in a blue filtered image. Because of this, not just red filtered SEM-CL images were made but also green and blue filtered, so that each filter could be looked at individually and as a composite RGB image. A small part of the 1024 sample is shown in figure 4. It depicts a blue, red and green filtered SEM-CL image, and a RGB composite image of the 3 filtered images combined together in Photoshop. The images show some large grains that have not been recrystallized (red) surrounded by recrystallized grains (blue). Some of the larger non-recrystallized grains show distinct subgrain boundaries. The large grain inside the red circle on the blue filtered image is an example of this. Unlike the naturally deformed samples, in this experimentally deformed sample the subgrain boundaries are best defined in blue filtered images. The green filtered image depicts the same subgrain boundaries, but here they are much less defined. The red filtered image, which depicts the subgrain boundaries the clearest in all the Cap de Creus samples, does not show any sub-gain boundaries in this sample at all. The composite image confirms this observation by showing that the subgrain boundaries appear less red than the surrounding grain. Another noticeable feature in the images in figure 4 is that the recrystallized grains all have a blue colour while the non-recrystallized grains all show an orange-red colour.

For all four samples multiple SEM-CL images were taken adjacent to each other so they could be combined together in post processing of the images. This was done to depict a larger measured area while still keeping the magnification that best depicts the subgrain boundaries. This larger area makes for easier comparison between the SEM-CL images and images obtained from other imaging methods. All of these combined images are shown in appendices 2a-f. For sample 1024 not only the red filtered SEM-CL composite image is shown in the appendix, but also the blue filtered and the RGB composite image.

Electron microprobe

While the electron microprobe collects the complete spectrum at once, maps depicting the emission intensity in the red wavelength range (~595-850) were predominantly used to determine subgrain boundaries, since it still gives the strongest contrast between subgrain boundaries and the surrounding grains. However, maps depicting the emission intensity in the blue (~200-495) and green (~500-595) wavelength ranges were taken into consideration as well if they depicted any possible subgrain boundaries. Figure 5 shows all three maps by side together with the composite RGB image. In this image the maps that depict green and red wavelength emission intensity also depicts the

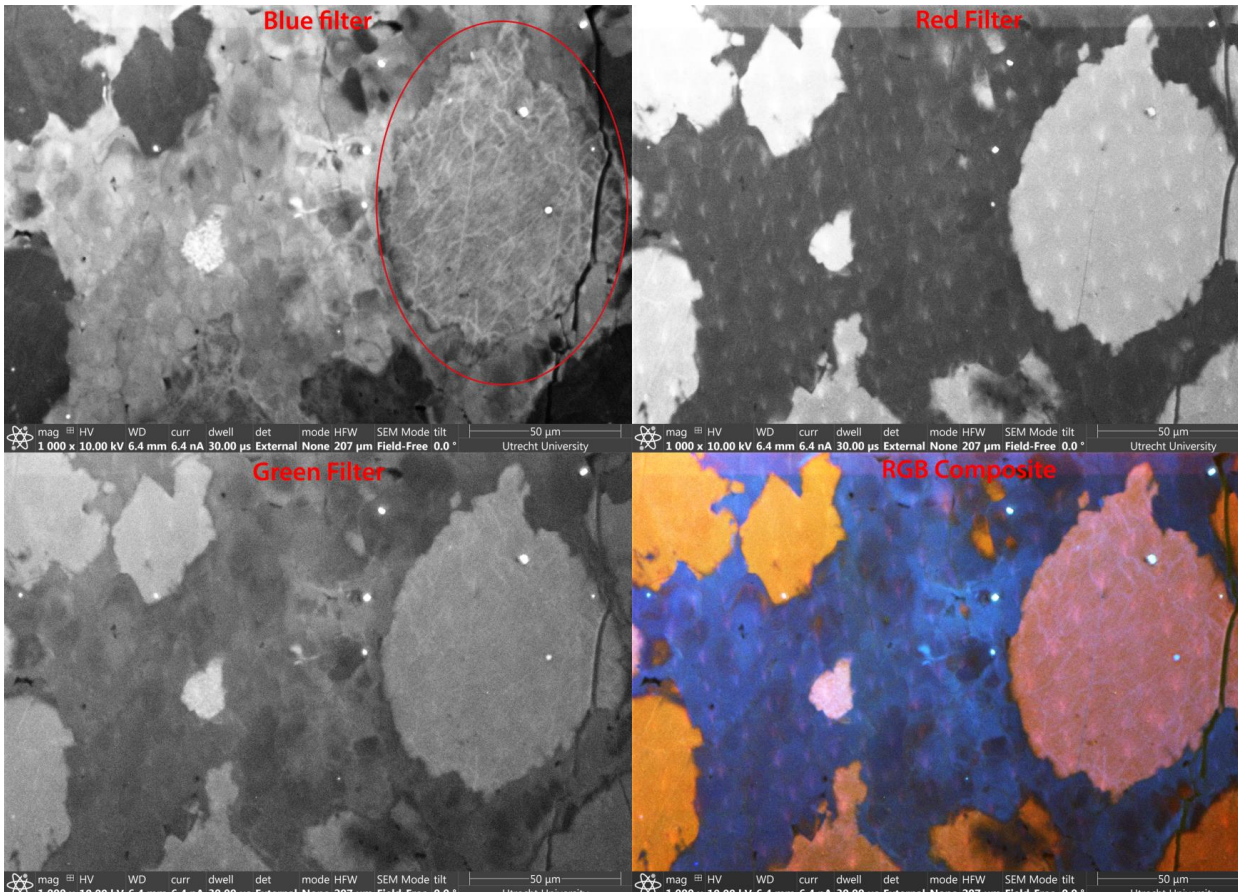

Figure.4 SEM-CL images of sample 1024 made with the RGB colour filters separate, after which they have been combined into a colour image with the use of Photoshop. The red circled grain shows distinct subgrain boundaries mostly located along the edges of the grain. The same grain in the green filtered image shows the same subgrain boundaries only they are significantly less distinct. The red filtered image shows no subgrain boundaries at all in the same grain. The subgrain boundaries are also visible in the RGB composite image where they show up as blue. The bright equally spaced dots in the red filtered image are caused by previously done EBSD mapping on this sample. The recrystallized grains show up blue on the composite image corresponding to their relatively bright colour in the blue filtered image. Similarly the non-recrystallized grains are orange-red in the composite image, which corresponds to their relatively bright colour in the red filtered image.

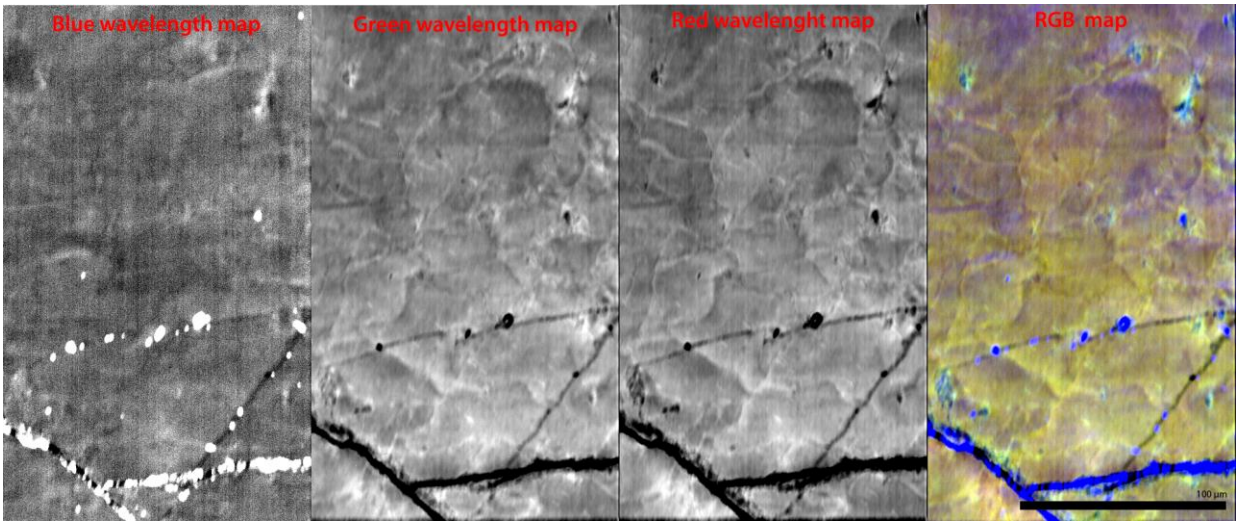

Figure.5 Electron microprobe maps of sample CC98-4. The maps depicting the red and green wavelength emission intensity both show well defined subgrain boundaries. The map depicting the blue wavelength emission intensity only depicts them partially or not at all. This results in the subgrain boundaries being yellow-orange in the composite map. The bright blue colour, seen in cracks and holes in the sample, is most likely the result of the polishing material used (Al_2O_3). The black bar in the bottom right is 100µm.

subgrain boundaries with high relative contrast. The bright blue colour that the microprobe measured inside some of the cracks and holes in the sample is most likely polishing material, since the polishing material used was Al_2O_3, which has a strong blue luminescence *(Hamers et al., 2016).* This bright blue only occurs in the CC98-4 and CC98-4c samples. The 1024 sample no longer shows the subgrain boundaries in map depicting the blue wavelength emission intensity instead depicts them most clearly in the maps depicting red and green wavelength intensity just as the other samples.

To compare the visibility of the subgrains and the number of subgrains detected in the microprobe to what was measured in the SEM-CL images, the subgrain boundaries in the microprobe image were manually traced. Different automated methods were explored. However, due to contrast differences between the top and bottom of the image for example it was impossible to threshold the images so that only the slightly brighter subgrain boundaries would be included into an image. Because of this, manually tracing the subgrain boundaries was the only viable option for comparison between different detection methods. Figure 6 shows the same map depicting the red wavelength emission intensity of sample CC98-4 as figure 5, before and after the subgrain boundaries were manually traced. Figure 7 shows these traced subgrain boundary lines layered on top of the SEM-CL red filtered image of the same area in sample CC98-4. Larger versions of these images can be found in appendices 3a-d. In the manual tracing of these subgrains a distinction had to be made between which lines are subgrain boundaries and which are not. Because this is done manually there is always a risk of some error or opinion bias involved.

In figure 7b it is visible that the traced subgrain boundaries taken from the electron microprobe map don't depict all the subgrain boundaries that are visible in the SEM-CL image. A clear example of this is inside the blue circle in figure 7b. There are clear subgrain boundaries visible in this circle that are unclear or don't show up at all in the electron microprobe map in figure 6. When comparing the SEM-CL image to the electron microprobe map, the SEM-CL image shows a clearer contrast between the subgrain boundaries and the surrounding grains. The electron microprobe map shows more varied shades of grey all across the sample, which makes it harder to distinguish between actual subgrain boundaries and other relatively lighter areas. The overall image quality also looks more blurred in the electron microprobe map compared to the SEM-CL image; this blurred effect also results

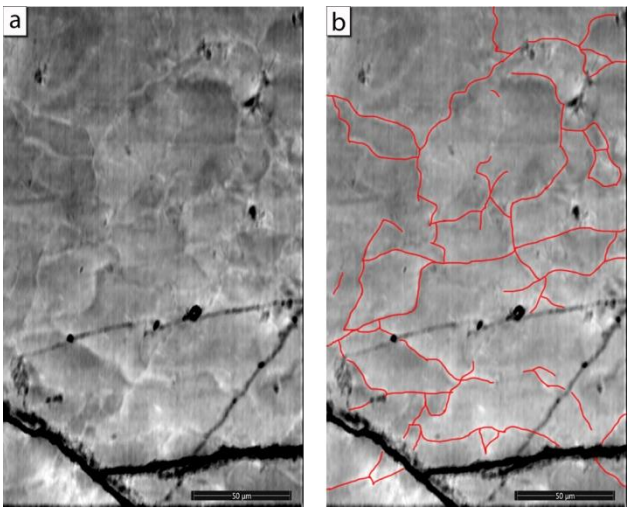

Figure.6 Electron microprobe map depicting the red wavelength emission intensity of sample CC98-4. 6a shows the map as it was taken. In 6b all the clear subgrain boundaries are traced in red. The black bar in the bottom right of each image is 50µm

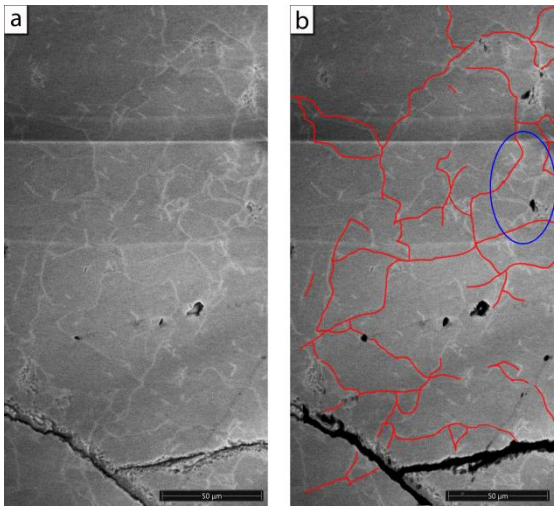

Figure.7 SEM-CL red filtered image of sample CC98-4. The images show the same area as is depicted in figure 6. The left image is the unaltered image. The bright horizontal line through the image is where 2 adjacent SEM-CL images are attached together. 7b shows the overlap between the traced lines from the microprobe map in figure 6b, and the SEM-CL red filtered image in 7a. The blue circle shows an example area of subgrain boundaries in the SEM-CL image that have not been picked up by the microprobe. The black bar in the bottom right of each image is 50µm.

in the cracks inside the sample appearing much larger in the microprobe map than in the SEM image.

The data obtained by the electron microprobe can also be used to visualise the CL spectra of the different samples. Figure 8 shows the CL spectrum of sample CC98-4. Figure 8a depicts the CL spectrum of inside a grain, while Figure 8b depicts the CL spectrum on the subgrain boundaries. Both the CL spectra taken from within the grain and the one taken from subgrain boundaries depict the same three peaks. The only difference between the two CL spectra is that the peaks at ~1.955eV and ~1.870eV have a higher intensity in figure 8a than in figure 8b. These eV values correspond to a red wavelength of ~634nm and ~663nm respectively. This increase in red wavelength intensity at the subgrain boundaries corresponds with the observation that these boundaries show up brighter in a red filtered SEM-CL image. The final peak at ~2.375eV has a relatively low intensity and a similar intensity in both figure 8a and b.

Figure 9 depicts the CL spectrum of sample CC98-4c, with 9a being measured inside a grain and 9b being measured at subgrain boundaries. Both 9a and 9b depict the same four peaks. Of these, the peaks at ~1.955eV and ~1.870eV are also measured in figure 8. However unlike in figure 8, in this case the ~1.955eV and ~1.870eV peaks are less intense in the subgrain boundaries than in the grains. This does not correspond to observations made during SEM-CL measurements where the subgrain boundaries appeared brighter in a red filtered image and not darker. The other two peaks present at ~2.06eV and ~2.9eV have a relatively low intensity and are similar in intensity when comparing 9a to 9b.

Figure 10 depicts the CL spectra of sample CML-2. Figure 10a depicts the spectrum taken from inside grains while figure 10b depicts the spectrum taken at the subgrain boundaries. This sample depicts four peaks that are in similar locations in both 10a and 10b. Out of these 4 peaks, the peak at ~3.12eV is the weakest. This peak is slightly more intense in 10a than in 10b. The peaks at ~1.955eV and ~1.870eV are again measured in this sample. And much like in figure 8, they have a higher intensity when measured at subgrain boundaries than when measured inside grains. This again corresponds with the observation that these boundaries show up brighter in a red filtered SEM-CL image. The last peak at ~2.79eV does not significantly increase or decrease between figure 10a and figure 10b.

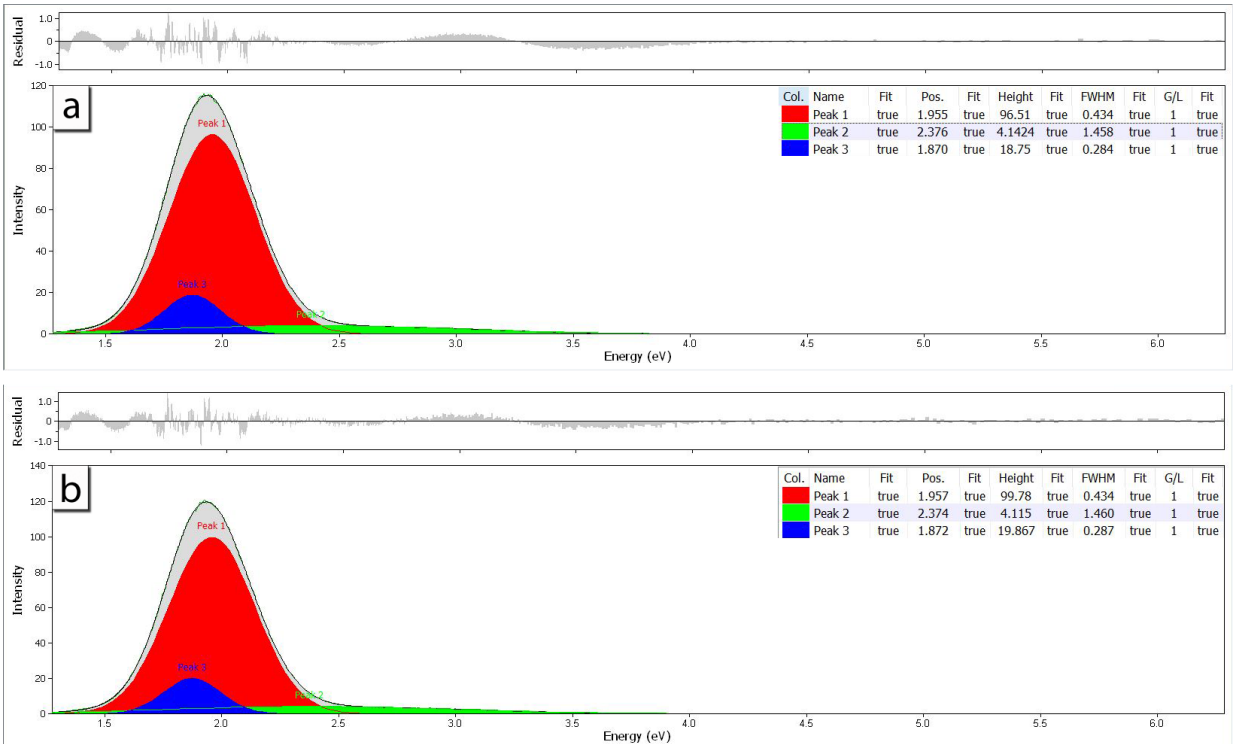

Figure.8 Both a and b depict CL spectra of sample CC98-4. 8a depicts the CL spectrum measured inside grains while 8b depicts the CL spectrum measured at the subgrain boundaries. The top right of each image has a legend that indicates the location and intensity of each peak.

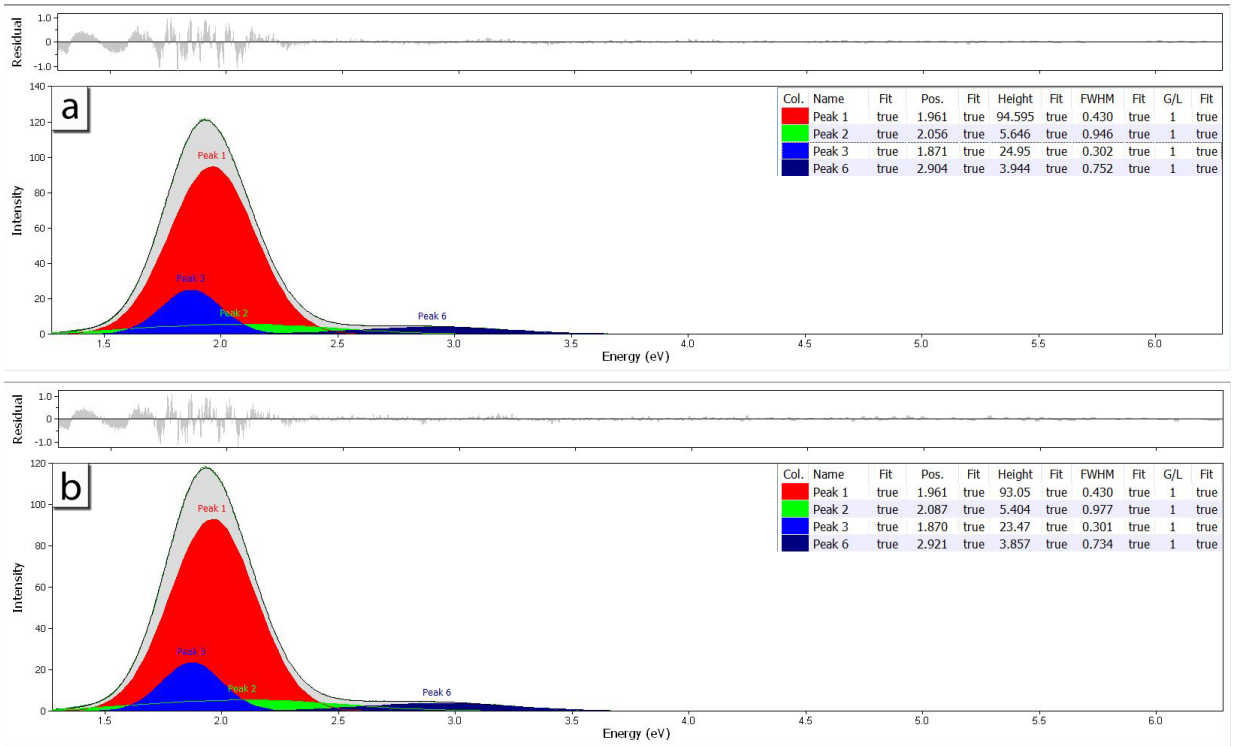

Figure.9 Both a and b depict CL spectra of sample CC98-4c. 9a depicts the CL spectrum measured inside grains while 9b depicts the CL spectrum measured at the subgrain boundaries. The top right of each image has a legend that indicates the location and intensity of each peak.

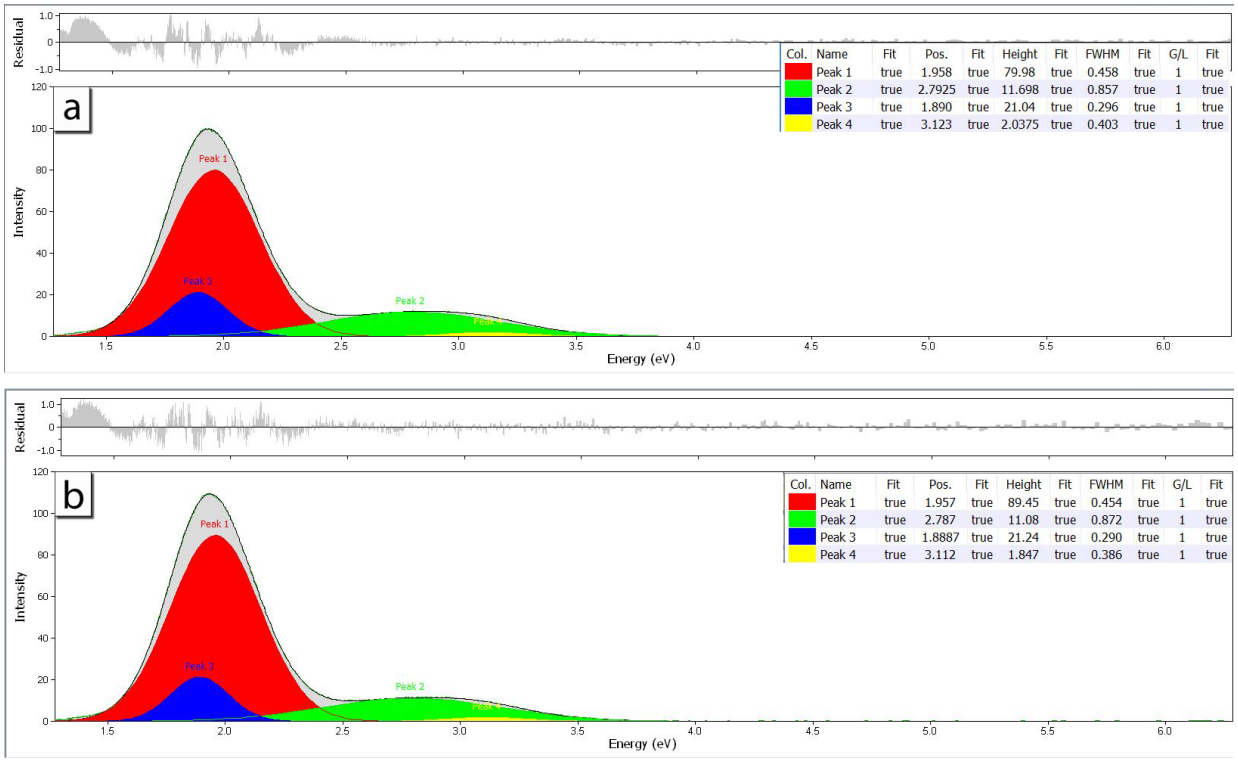

Figure.10 Both a and b depict CL spectra of sample CML-2. 10a depicts the CL spectrum measured inside grains while 10b depicts the CL spectrum measured at the subgrain boundaries. The top right of each image has a legend that indicates the location and intensity of each peak.

Figure 11 depicts the CL spectra of sample 1024. In this figure 11a depicts the CL spectrum taken from inside the recrystallized grains that are shown in a blue colour on the composite SEM-CL image of sample 1024. Figure 11b depicts the CL spectrum taken from inside regular non-recrystallized grains and figure 11c depicts the CL spectrum taken at the subgrain boundaries. All three spectra show the same four peaks, only figure 11a has an extra peak at ~3.141eV with a low intensity. The peak at ~1.955eV that is measured in all the samples so far is also measured in this sample. This peak is stronger when measured at the subgrain boundaries (11c) than when measured in the normal grains (11b). This same peak also occurs in the recrystallized grains (11a) but is much weaker here than those measured in 11b and c. All of the other peaks also show a weaker intensity in 11a than in the other two CL spectra. The peaks at ~2.2eV and ~2.15eV both show a slightly higher intensity in figure 11c than in figure 11b. The peak at ~2.96eV does not show a significant increase between b and c. The observation that subgrain boundaries in sample 1024 are best depicted with a blue filtered SEM-CL image, and cannot be seen in a red filtered SEM-CL image, does not correspond with the increase in intensity of the ~1.955eV when measured at subgrain boundaries. This peak corresponds to a red wavelength and thus the subgrain boundaries would be expected to be brighter in a red filtered SEM-CL image. The large decrease in intensity of the ~1.955eV peak in figure 11a, corresponds with the recrystallized grains being depicted more blue than the surrounding normal grains in the SEM-CL image of sample 1024.

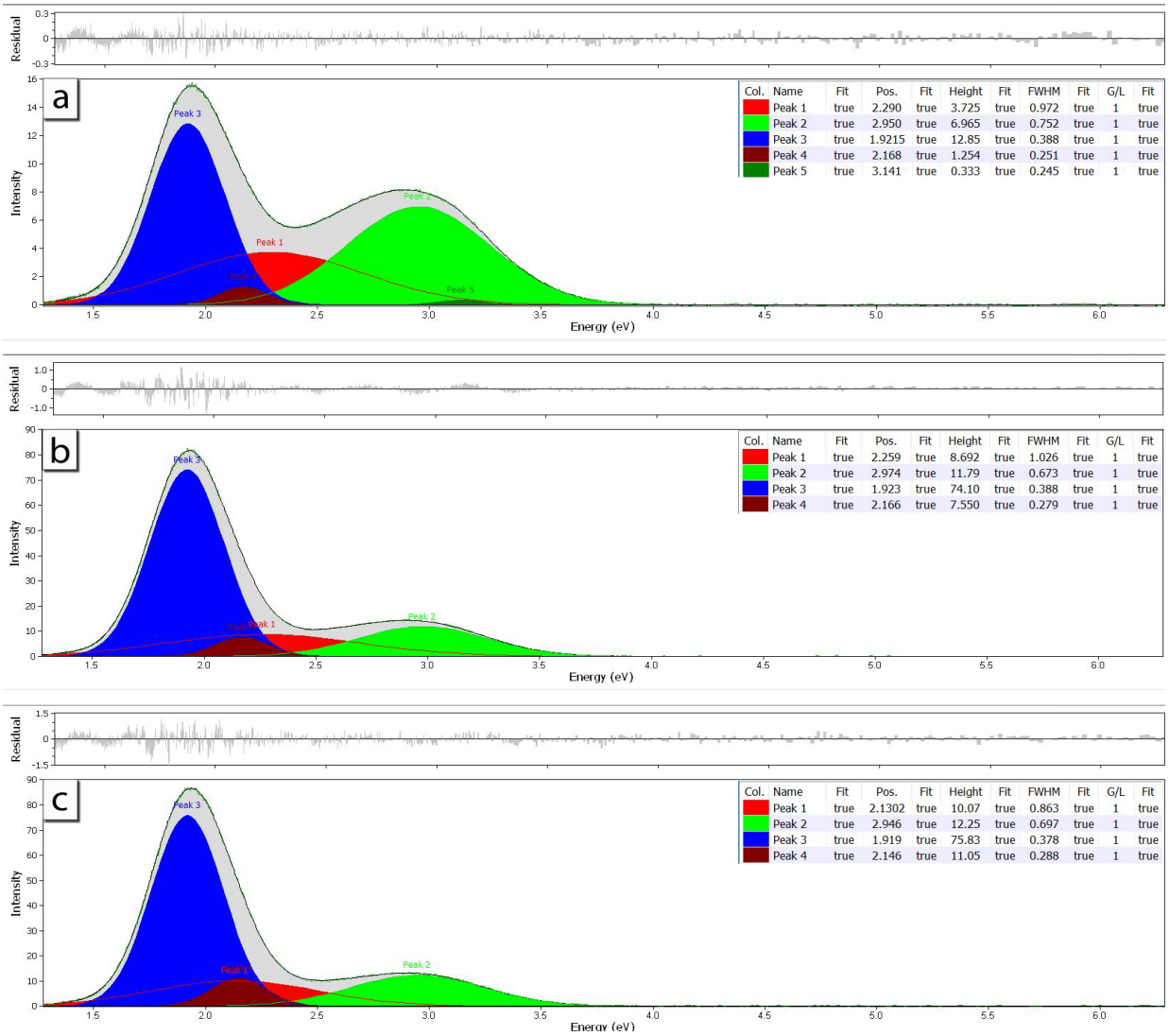

Figure.11 Both a, b and c depict CL spectra of sample 1024. 11a depicts the CL spectrum measured inside recrystallized grains. 11b depicts the CL spectrum measured in non-recrystallized grains and 11c depicts the CL spectrum measured at the subgrain boundaries. The top right of each image has a legend that indicates the location and intensity of each peak.

EBSD

EBSD can measure the angular difference between different measurement points. Because of this EBSD can be used to distinguish between subgrain boundaries, normal/recrystallized grain boundaries and Dauphiné twins. Figure 12 shows an EBSD map taken from a small part of sample CC98-4. The green lines in this case show the smallest angular difference between subgrains with angles between 1^{o} and 2^{o}. These lower degree angles become progressively harder to detect for the EBSD at around 0.7^{o} *(Pennock et al., 2002; Brough et al., 2006)*. The yellow lines indicate all other subgrain boundaries. These other subgrain boundaries have an angular difference between 2^{o} and 10^{o}. Above 10^{o} the boundaries won't be considered subgrain boundaries anymore but just normal grain boundaries. These normal grain boundaries are depicted by the black lines. The red lines indicate Dauphiné twins; they have an angular difference of 60^{o} with a rotation axis parallel to [0001] with an error margin of 5^{o} on each side, so any boundary between 55^{o} and 65^{o} is considered a Dauphiné twin.

Figure 13 shows the difference between different EBSD data processing settings and subgrain boundary definitions when compared to a SEM-CL image of the same area in sample 1024. Figure 13a shows that in the SEM-CL blue filtered image most subgrain boundaries are visible in the larger non-recrystallized grains. Figure 13b, which is the same in settings as figure 12, shows that these settings are well suited for showing grain boundaries and Dauphiné twins, but the parameters of the low angle subgrains are not enough to register all the subgrain boundaries that are visible in the SEM-CL image. In figure 13c, the parameters of the green lines are adjusted so that it now indicates angular differences between 0.5^{o} and 2^{o}. As a result of this change the EBSD data depicts more of the subgrain boundaries than it did before. These boundaries however, are less clear with a lot of 1 or 2 pixel wide mini subgrains that are unlikely to actually be present. To alleviate this problem and clean the image up more, the Kuwahara filter was applied to the image twice, which resulted in figure 13d *(Brough et al., 2006)*. The detected subgrain boundaries are the same as figure 13c, only now most of the 1 pixel subgrains have been removed. The EBSD data of figure 13d, while better than the previous images, still does not detect all the visible subgrain boundaries in the SEM-CL image. Figure 13e, which has undergone the same cleaning and filter process as 13d, now has the parameters of the green boundaries set to include all angular differences between 0.4^{o} and 2^{o}. As a result this figure depicts more subgrain boundaries than any of the previous figures, but still not all subgrain boundaries visible in the SEM-CL image are detected by the EBSD. In Figure 13f, all settings remain the same once again, only the parameters for the green boundaries have again been increased to now include all angular differences between 0.3^{o} and 2^{o}. At this point most of the visible subgrain boundaries in the SEM-CL image are detected by the EBSD data. However, at this point some 1 or few pixel subgrains start to show up again. Because of this it is unadvisable to set the parameters of the green lines to include even lower angled subgrain boundaries.

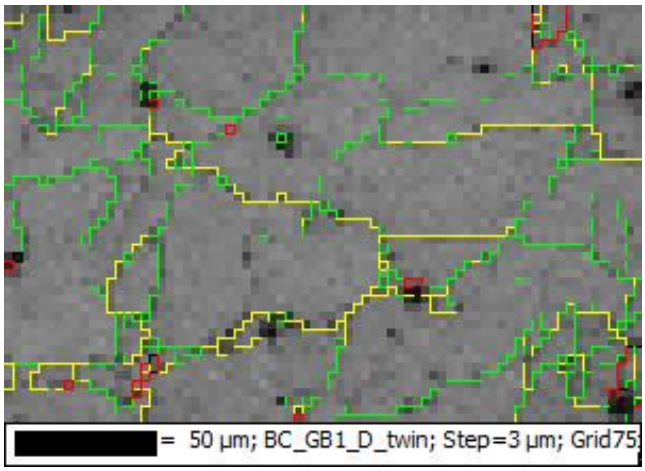

Figure.12 An EBSD image taken from sample CC98-4. The EBSD data has undergone wildespikes removal and iterative cleaning up to 5 adjacent neighbours. The green lines indicate an angular difference between 1^{o} and 2^{o}. The yellow line indicates an angular difference between 2^{o} and 10^{o}. The black lines indicate an angular difference of larger than 10^{o}, with an exception of an angular difference between 55^{o} and 65^{o}, which are indicated with a red line.

By combining the SEM-CL imaging with EBSD a dataset can be made that includes all the low angle grain boundaries but also filters out the normal grain boundaries and Dauphiné twins. This is done by filtering out just the normal grain boundaries and Dauphiné twins, which are symbolized by black and red lines respectively, and placing them on top of the corresponding SEM-CL images (figure 14) much like it is done in figure 13. The resulting

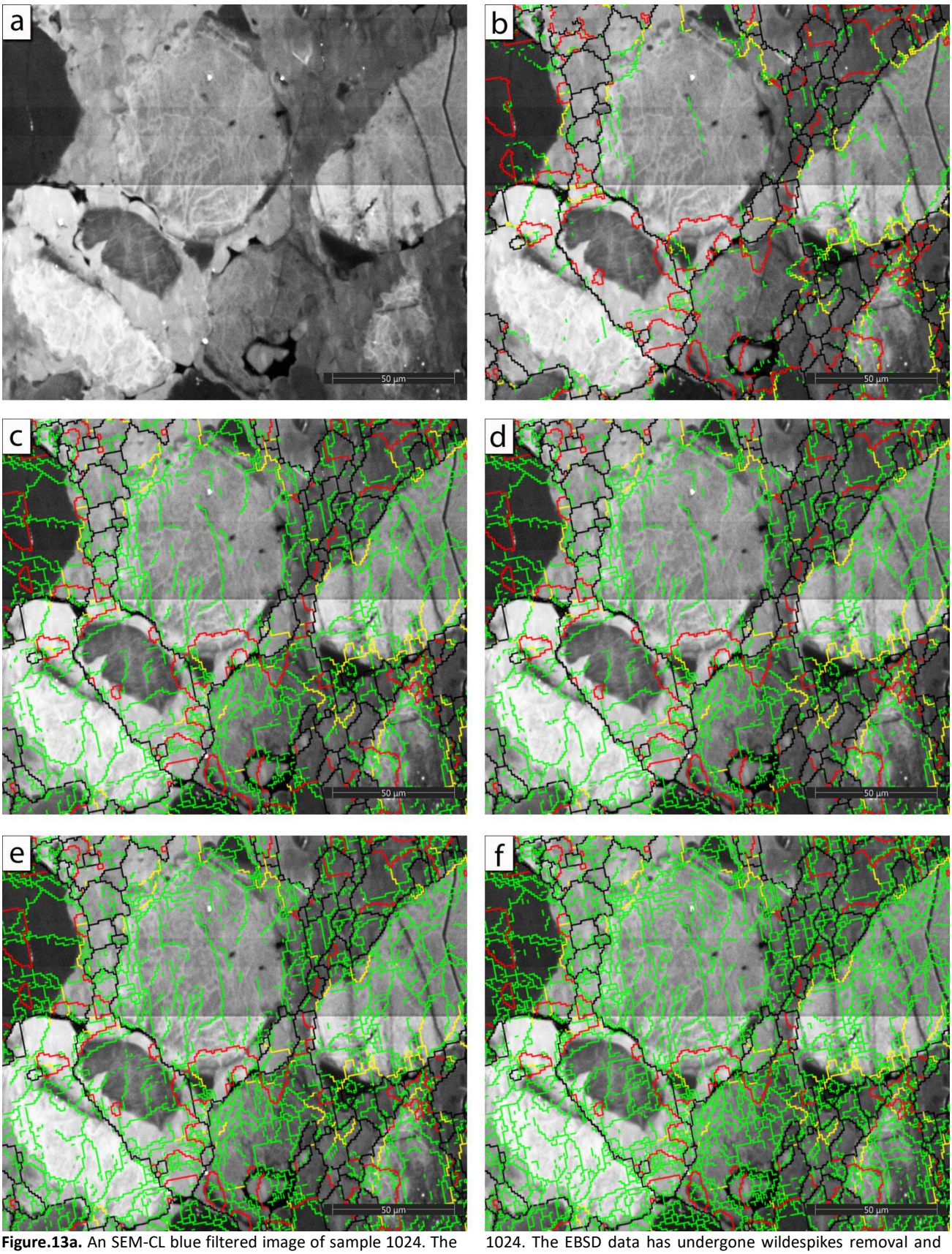

Figure.13a. An SEM-CL blue filtered image of sample 1024. The subgrain boundaries are predominantly visible in the larger non-recrystallized grains. All images in this figure are taken in the exact same location as this one. **b.** EBSD (sub)grain boundary lines placed on top of SEM-CL blue filtered image of sample 1024. The EBSD data has undergone wildespikes removal and iterative cleaning up to 5 adjacent neighbours. The coloured lines indicate the same angular difference as in figure 12. **c.** Same as 8b, only now the green lines indicate an angular difference between 0.5° and 2°. **d.** EBSD (sub)grain boundary lines placed on top of SEM-CL blue filtered image of sample 1024. The EBSD data has undergone wildespikes removal and iterative cleaning up to 3 adjacent neighbours after which a Kuwahara filter was applied twice with a 3x3 matrix, a smoothing angle of 5° and an artefact filter of 1°. The coloured lines indicate the same angular difference as in figure 12 with the only exception being the green line which indicates an angular difference between 0.5° and 2°. **e.** The same as 8d, except for the green lines, which show an angular difference between 0.4° and 2°. **f.** same as 8d, except for the green lines, which show an angular difference between 0.3° and 2°.

image, as can be seen in figure 14, can be used to manually apply the linear intersect method on the SEM-CL subgrain boundaries without having to worry about counting Dauphiné twins or normal grain boundaries as subgrain boundaries. Since normal grain boundaries, recrystallized grain boundaries and Dauphiné twins all have misorientation angles of larger than 10°, EBSD should have no trouble detecting all of them in a sample. This method is only used on samples CML-2 and 1024, because the CC98-4 and CC98-4c SEM-Cl data was taken in a location with no normal grain boundaries and Dauphiné twins present. As can be seen in figure 14 it sometimes occurs that the parameters set to detect the Dauphiné twins don't pick up the entire twin. In these cases it can occur that the red line, that indicates the Dauphiné twin, transitions into a black line, which indicates any angular misorientation larger than 10°, and then back to red. In these cases it is assumed that the black line is still part of the Dauphiné twin boundary.

Paleopiezometry

For all the different data acquisition methods discussed in this thesis, subgrain diameter measurements were taken by manually applying the linear intersect method on the acquired images. Table 1 shows the average subgrain linear intercept measured per sample for each data acquisition method. All the subgrain diameter measurements were taken with the use of the program ImageJ. Table 1 shows the average grainsize for all 4 samples with each different data acquisition method. The largest subgrain sizes across all samples have been measured with the use of light

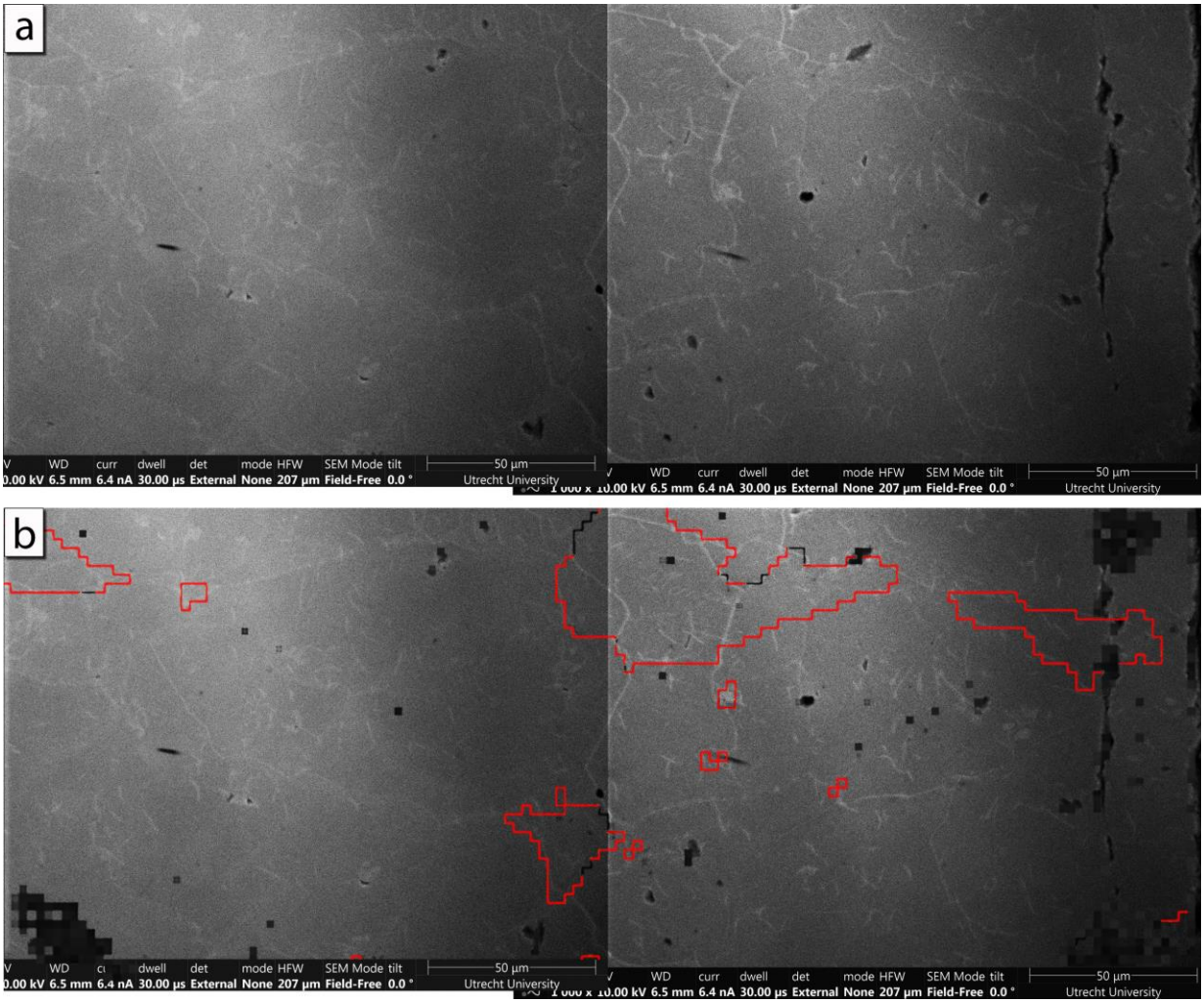

figure.14 A SEM-CL red filtered image of sample CML-2. Figure 14a is 2 SEM-CL red filtered images attached to each other, with the stark brightness difference line down the centre being the location where they were attached. Figure 14b depicts the same SEM-CL image with overtop the EBSD data indicating the normal grain boundaries and Dauphiné twins.

microscopy. Light microscopy has been used more as a check than as an actual contender for the best method to detect subgrain boundaries. After these the largest subgrain diameter sizes are measured in the electron microprobe images and in the manually measured EBSD images. The reason there is no subgrain size data for the CML-2 electron microprobe data, is because the area that was measured with the electron microprobe did not show enough subgrain boundaries to make an accurate average measurement. When the automatic linear intersect method, that comes with the channel 5 Tango program, is used to measure the average subgrain sizes, they are smaller than the manually measured ones. The smallest manually measured subgrains are measured by using the data obtained from SEM-CL imaging. This would indicate that the SEM-CL imaging shows the most subgrain boundaries out of all data acquisition methods used in this thesis. However SEM-CL does not account for possible normal grain boundaries and Dauphiné twins. This leads to the subgrain size measurements measured in the SEM-CL data being smaller than the actual average subgrain sizes would be. The combined SEM-CL and EBSD data average subgrain sizes are slightly larger than those from the sole SEM-CL data, but are still significantly smaller than the average subgrain sizes from the sole manual EBSD data. This method was only used for samples CML-2 and 1024 since the samples CC98-4 and CC98-4c don't show enough normal grain boundaries and Dauphiné twins in the location where the SEM-CL image was taken to have an influence on the subgrain size measurements.

When comparing the different samples to each other, 1024 clearly has the smallest subgrain size by far followed by CC98-4c. CC89-4 and CML-2 have similar, relatively larger average subgrain sizes. To calculate stress estimates from this subgrain sizes, a piezometric relationship has to be used. for this thesis the piezometric relationship described in (Goddard et al., T.B.D.) was used. This is:

$$\frac{\lambda}{b} = 10^{0.77\pm0.63}\left(\frac{\sigma_1-\sigma_3}{\mu}\right)^{-1.18\pm0.24}$$

"Where λ is the mean intercept length in µm, b is the burgers vector in µm, (σ 1 – σ 3) is the equivalent flow stress (MPa), and µ is the shear modulus (MPa)." *(Goddard et al., T.B.D.)*. The burgers vector for quartz was taken to be 5.10 x 10^{-4}µm and the shear modulus 4.2 x 10 4 MPa. *(Goddard et al., T.B.D.).* Combining this piezometer with the measured subgrain values results in the stresses that are depicted in table 2. To see if these stress estimates are accurate, they have to be compared to stress estimates based on the recrystallized grainsize of the different samples. To do this, the recrystallized grainsize was measured with light microscopy and then combined with the piezometer taken from Stipp and Tullis (2003). This piezometric relationship is:

$$D = 3631\sigma^{-1.26}$$

Where D is the recrystallized grain size and σ the stress. Only the piezometric relationship that can be applied to regimes 2 and 3 (as defined in Stipp and Tullis (2003)) is used. This is done because none of the measured grain sizes, as shown in table 3, are below ~3µm. At around 3µm the transition occurs from regime 2 into regime 1. This renders the piezometric relationship for regime 1 unnecessary as all samples are outside this regime. Table 3 shows the stress estimates resulting from the recrystallized grainsize piezometer. Comparing the recrystallized stress estimates from table 3 with the stress estimates from table 2 shows that the light microscopy subgrain estimates don't come close to the stress values calculated with the recrystallized grain stress estimates. The measurement technique that comes closest to the stresses calculated in table 3 is the EBSD measurement combined with the automatic linear intersect method that can be used by the program channel 5. After this the closes stress estimates come from the SEM-CL measurement techniques, followed by the combination of SEM-CL with EBSD measurements to filter out the Dauphiné twins and regular/recrystallized grains. After this the next closest detection method in terms of stress estimates is the EBSD combined with manually applying the linear intersect method. The non-light microscopy method that was furthest away in its stress estimate from the stress values calculated in table 3 is the electron microprobe.

Average subgrain diameter in µm	CC98-4	CC98-4c	CML-2	1024
Light microscopy	53.5743	114.2336	143.955	12.76018
SEM-CL	20.8978	13.11975	22.02543	4.552147
Electron microprobe	23.20465	21.40062	x	5.538583
EBSD channel 5	12.67678	12.84152	16.58428	3.986773
EBSD manual	22.3977	20.01572	27.24714	5.83841
SEM-CL + EBSD	x	x	24.13862	4.864371

Table.1 Average subgrain diameter measurements in µm. The top row indicates which sample was measured and the left column indicates which data acquisition method was used.

Stress in Mpa	Light microscopy	SEM-CL	Electron microprobe	EBSD channel 5	EBSD manual count	SEM-CL + EBSD
CC98-4	10.48044009	23.27381629	21.29756387	35.55032596	21.94606779	x
CC98-4c	5.517010272	34.53046923	22.80956344	35.16343868	24.14015246	x
CML-2	4.535144964	22.26000723	x	28.31103266	18.58759886	20.59712931
1024	35.35331289	84.68110801	71.71301861	94.75358656	68.57956127	80.05176066

Table.2 Stress estimates based on average measured subgrain sizes and the piezometer for subgrains taken from Goddard et al., T.B.D. the top row indicates what subgrain measuring method was used. the left column indicates which sample was measured.

	Light microscopy, recrystallized grainsize (µm)	Stress (Mpa) based on Stipp and Tullis(2003)
CC98-4	40,8746	35,19543167
CC98-4c	80,96414	20,45971766
CML-2	60,9101	25,64469679
1024	11,6	95,63342943

Table.3 Average recrystallized grainsize measurements in µm and stress estimates based on the average measured recrystallized grain sizes and the piezometer for recrystallized grains taken from Stipp and Tullis (2003) The left column shows which sample the measurements are from. The top row indicates what was measured or calculated

Discussion

SEM-CL

The SEM-CL images show clear and distinct bright lines that could either be subgrain boundaries or Dauphiné twins. In three of the four samples studied these lines show up most clearly in a red filtered CL image, corresponding to *Hamers, et al., 2016*. However, this is not always the case, in sample 1024 these bright lines show up better in a blue filtered image. The SEM-CL images often show shadows across the images as can be seen in figure 2 and figure 15. Because of this shadow, which makes some parts of the image darker than others, it is was not possible to use image thresholding to detect all the bright lines automatically, and thus this had to be done by hand. Because the bright lines in the SEM-CL images are so clear and distinctly lighter than the grains around them, they were easy to detect manually. If SEM-CL images were made without a shadow it would be an easy process to threshold the image with programs such as imageJ to automatically detect every single bright line. SEM-CL imaging is by far the fastest method out of the three tested methods for detecting possible subgrain boundaries and Dauphiné twins, with a single image as shown in figure 15 being taken in minutes instead of an hour or more. This is in the case of taking an image with a single colour filter. If a full colour image has to be made, this takes closer to 15-30 minutes as each colour filter image has to be taken separately and then combined into a full RGB false-colour image.

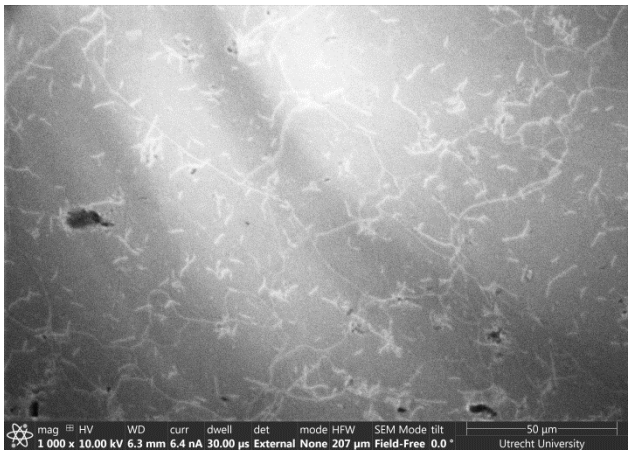

Figure.15 SEM-CL red filtered image of sample CC98-4c. The relatively bright lines are possible subgrain boundaries or Dauphiné twins and the black spots are either holes in the sample or dirt on the surface of the sample. The image shows shadows cast over the SEM-CL image. These shadows are most likely caused by the CL detector. Because of these shadows it was impossible to use image thresholding to clearly pick up all the bright lines. As for example the bright lines in the bottom right of the image are darker than the normal grains located at the top of the image.

Electron-Microprobe

The electron microprobe depicts the possible subgrain boundaries and Dauphiné twins in the same way as the SEM does. With the possible subgrain boundaries or Dauphiné twins being best depicted by a map which depicts the emission intensity in the red wavelength range where they show up as bright lines. The time it takes for the electron microprobe to record hyperspectral CL maps, takes significantly longer than the SEM-CL images, with the electron microprobe making a map the size of about 1.5 SEM-CL images in multiple hours compared to the few minutes it would take to cover the same area with SEM-CL imaging. These times can vary depending on things like used step size, dwell time and beam settings, but for the purposes of accurately detecting possible subgrain boundaries, the SEM-CL is significantly faster. However, the microprobe collects the complete spectrum in each point of a map, after which the user defines what colours are used to make each image. In the maps made by the electron microprobe the possible subgrain boundaries and Dauphiné twins are still visible as bright lines but they are less clear and distinct than they were in the SEM-CL images. The bright lines often show up blurry and covering a wider area than they would in the SEM-CL images. The grains themselves also show up in multiple shades of grey unlike the homogenous grey colour in the SEM-CL images. This also makes the relatively bright lines harder to detect. This discrepancy is most likely the result of the different measurement techniques. The electron microprobe has a step size of 0.3µm while the SEM-CL image depicts 0.067µm per pixel. This means that the SEM-CL can show a much clearer picture with better defined subgrains than the electron microprobe can.

When comparing the SEM-CL method to the electron microprobe method, for detecting possible subgrain boundaries and Dauphiné twins, the SEM-CL imaging method is both faster and better depicts these micro structures. Figure 7 also shows that the SEM-CL imaging actually picks up more of the possible subgrain boundaries and Dauphiné twins

than the electron microprobe did. It is possible that if the step size in the microprobe was set to smaller increments it would give just as clear of a picture as the SEM-CL does. This however, would increase the time it takes to make a map even more. The main advantage of the electron microprobe is that it measures CL spectra and can measure chemical compositions along with it. This is however not necessary for subgrain boundary detection as these show up clearest in selected wavelength maps (predominantly in the red range).

CL-spectra

There are two peaks that are predominant troughout all four samples (figure 8 until 11). These are the peaks at ~1.955eV and ~1.870eV which correspond to a wavelength of ~634nm and ~663nm respectively. Hamers et al. (2016) explained the red signal of subgrain boundaries by the concentration of defects that produce the red emission along the boundaries. The defects that would best explain these peaks and thus the red signal are non-bridging oxygen holes (*Götze et al., 1999, 2001).* In samples CC98-4 and CML-2 these peaks at ~1.955eV and ~1.870eV show a higher intensity when measured at subgrain boundaries (figures 8 and 10), than when measured inside the grains. This increase in intensity at subgrain boundaries corresponds with the observation that the subgrain boundaries show up brighter than the surrounding grains in a red filtered SEM-CL image. This also corresponds with the findings of Hamers et al. (2016).

Sample CC98-4c also depicts the subgrain boundaries as brighter compared to the surrounding grains in a red filtered SEM-CL image (figure 9). However, the spectra of sample CC98-4c show a decrease in intensity of the peaks at ~1.955eV and ~1.870eV when measured at subgrain boundaries. All other peaks measured in sample CC98-4c also show a decrease in intensity when measured at the subgrain boundaries. A possible explanation for this overall reduction in intensity at subgrain boundaries, is that the multiple scans that have been taken of the sample up to this point have caused beam damage to the sample. The sample could have been damaged to such an extent that the CL signal has started to become weaker. It stands to reason that the subgrain boundaries are one of the first places to be affected by this beam damage, because the dislocation density is higher at these locations and thus the crystal structure weaker.

Sample 1024 shows the opposite situation of sample CC98-4c. In SEM-CL imaging the subgrain boundaries in this sample are best distinguished in a blue filtered image and non-distinguishable in a red filtered image. However, figure 11 does show that the sample experiences an intensity increase of the peaks at ~1.955eV and ~1.870eV when measured at subgrain boundaries. At this point it is not yet clear what might have caused this discrepancy. A possible reason could be the differences in scanning techniques between the SEM-CL and the electron microprobe. However, if this was the case, one would expect similar observations in the other samples which have undergone the same process. Further research will need to be done to make an accurate determination of what the cause is of this discrepancy between SEM-CL and electron microprobe data.

Figure 11a shows that the blue colour of the recrystallized grains is not caused by a large increase in intensity of peaks that correspond to a blue wavelength of 350-510nm (3.5-2.43eV). Instead, all peaks show a decrease in intensity, with by far the largest decrease in intensity measured in peaks that correspond to a red wavelength of 600-800nm (2.07-1.55eV). This large decrease in the peak at ~1.955eV can explain why the recrystallized grains look blue compared to the other non-recrystallized grains. This large decrease in the intensity of the peak at ~1.955eV is most likely caused by the fact that these newer recrystallized grains don't have as many defects yet as the non-recrystallized grains. Since the red CL signal is determined to be related to the concentration of defects in the grain *(Hamers et al., 2016)*, it seems likely that a younger grain, with less defects, would appear more blue than the surrounding older grains. There is also a small peak at ~3.141eV (~394.7nm), which is caused by aluminium content *(Götze et al., 2001)*. Aluminium can be incorporated into the quartz structure by substitution of Al^{3+} for Si^{4+} (*Götze et al., 2001).* This small peak by itself, would not be enough to make the recrystallized grains appear this bright in a SEM-CL blue filtered image.

EBSD

The EBSD measurements can only accurately

measure misorientation angles to no lower than ~0.5°, but with the use of post process clean-up methods this lower limit can be lowered *(Goddard et al., T.B.D.; Pennock et al., 2002; Brough et al. 2006)*. The subgrain boundaries (green lines) shown in figure 13e and f therefore give an uncertain image on if these lines are actually subgrain boundaries or Dauphiné twins and not artefacts from the measuring technique or clean-up methods. When comparing figure 13d, which has an angular misorientation range between 0.5° and 2° for the green lines, to figure 13e, where these green lines range between 0.4° and 2°, figure 13e shows significantly more subgrain boundaries. When comparing the EBSD lines to the underlying SEM-CL image in figure 13e, most of the green lines appear to correspond to bright lines that are also depicted in the SEM-CL image. It can therefore be assumed that even at a range between 0.4° and 2° the EBSD measuring method still has accurate results when it comes to measuring subgrain boundaries. When the angular misorientation range of the green lines is increased to include everything between 0.3° and 2° however, a lot of extra green lines are measured in the EBSD image that are not depicted in the SEM-CL image. This could be the result of either the SEM-CL image not detecting the lowest angular misorientations or because the EBSD starts to produce more artefacts at this subgrain boundary definition. Since EBSD analysis is known to have trouble with measuring these lower angle misorientations *(Goddard et al., T.B.D.; Pennock et al., 2002; Brough et al., 2006)* it is most likely that the extra lines are a result of the EBSD's limits on measuring low angle misorientations.

Taking EBSD measurements of a size large enough to detect enough subgrains for a stress estimate, and with a sufficiently small step size to measure the subgrain boundaries takes a large amount of time.

When comparing the EBSD data to the SEM-CL images (figure 13), the EBSD data, set with the green lines to include all angular misorientations between 0.4° and 2°, comes close to detecting all the subgrain boundaries that are visible in the SEM-CL image. The SEM-CL image still has some locations that show possible subgrain boundaries where the EBSD data doesn't show any, indicating that it can most likely show subgrain boundaries with a lower angular misorientation than the EBSD can detect, which corresponds with the findings of *Hamers, et al., 2016*. The time it takes to acquire the EBSD data is significantly longer than the time it takes to make the SEM-CL images. However, the big advantage of EBSD is that it can measure the actual angular misorientation. This means that unlike SEM-CL images a clear distinction can be made between subgrain boundaries, normal grain boundaries, and Dauphiné twins. To get the most accurate results for determining where subgrains are located and their size, the best option is to combine the SEM-CL image with the EBSD data. By using the EBSD data to filter out the normal grain boundaries and twins from the SEM-CL image, the best approximation can be made to the amount of subgrains and their size inside a sample area. When using EBSD to indicate Dauphiné twins in the SEM-CL images, the Dauphiné twins don't appear any brighter or less bright than the subgrain boundaries in the SEM-CL images (figure 14).

Paleopiezometry

As all (sub)grainsize measuring is done by hand without the use of any algorithms, following the linear intersect method, it comes with the possibility of errors made. This possibility of error lies entirely in the process of determining what should be considered a subgrain boundary and what not. The dislocation line had to be continuous to be considered a subgrain boundary. But even after using this rule to distinguish between what is a subgrain boundary and what isn't, the possibility for errors is still present. Using EBSD to filter out the normal grain boundaries and the Dauphiné twins from the SEM-CL image also improves the accuracy of the determination. Since all the measurements were made with the use of imageJ it is highly unlikely any measuring mistakes were made.

The decision to not try to automate the process of subgrain size measurement was made because there is no way to have a computer make the distinction between subgrain boundaries and Dauphiné twins or normal grain boundaries. Even if it were possible to make this distinction there would still be the issue of which normal grain boundaries to count and which to ignore. This is because in some cases normal grain boundaries have to be counted as they are also one of the boundaries of a subgrain located inside the overall larger grain. However in other cases the normal grain boundary can just be part of a small

recrystallized grains without any subgrain structures inside it, in these cases the normal grain boundary should not be counted when applying the linear intersect method. Because of this distinction it would be impractical for the process to be automated and instead applying the linear intersect method by hand has been chosen for.

Tango, the program used to process the EBSD images, does have a linear intersect option. However, this program also includes normal grain boundaries and counts the small 1 or 2 pixel subgrains that are constructed by the program. This gives a skewed result as can be seen in table 1. In the end, even with the possibility of human error, the best way to make a subgrain size estimate as accurate as possible, is by manually applying the linear intersect method on the SEM-CL image, which shows the most subgrain boundaries out of all three methods, and combining this with the EBSD image to filter out all the normal grain boundaries and any possible twins in the sample.

It is impossible to distinguish between all the different subgrains in light microscopy alone, depending on how close the extinction angles of two adjacent subgrains are together. If these angles are too close together the adjacent subgrains appear as a single larger subgrain making it most likely that the subgrain size value measured on light microscopy images are larger than the actual subgrain size would be. The measured average subgrain size for the SEM-CL data is most likely smaller than the actual subgrain size. This the result of the SEM-CL imaging not being able to distinguish between subgrain boundaries, normal grain boundaries or Dauphiné twins.

The recrystallized grain size stress estimate (table 3) made for sample 1024 is around ~7MPa less than the stress estimates made for the same sample by Stipp and Tullis (2003). This fits within the error margin of ~9MPa given in that paper. This lower estimate can be explained by the fact that the recrystallized grain size measurements in this thesis were made with the use of light microscopy, while the recrystallized grain size measurements in Stipp and Tullis (2003) were measured using SEM imaging. As discussed before SEM is more accurate than light microscopy. It is possible that the SEM would have picked up recrystallized grains that light microscopy did not. This would result in the measured recrystallized grainsize being smaller in Stipp and Tullis (2003) and thus the stress estimates to be larger. The measured grainsizes of the 3 naturally deformed Cap de Creus samples range from ~40-80µm. These values are similar to the values measured by Norton (1982). The resulting estimated stresses in this thesis also conform with stress estimates made by Norton (1982).

The piezometer of Goddard et al., (T.B.D.) was made using EBSD measurements. Without further research it cannot with certainty be said if this piezometer is fully applicable to other measurement techniques. The close proximity of the recrystallized grain stress estimates to the values of the subgrain stress estimates, seems to be indicating that this piezometer is usable for other measurement techniques. The measured subgrain sizes in the naturally deformed Cap de Creus samples, correspond to subgrain sizes measured in Norton (1982).

To arrive at the estimated stress values shown in table 2, the piezometric relation from Goddard et al., (T.B.D.) is applied to the average subgrain sizes in table 1. The piezometer from Stipp and Tullis (2003) is applied to the average recrystallized grain sizes in table 3 which results in the estimated stress values that are shown in the same table. When comparing the stress values estimated from subgrain sizes to the stress values estimated from recrystallized grain sizes it shows that the two subgrain stress estimates that come closest to the recrystallized grain stress estimate are the EBSD combined with automatic linear intersect method and the SEM-CL method. However, both these methods have been ruled out as the optimal method for subgrain detection due to the limitations discussed earlier in this discussion. After these two the method that combines SEM-CL with EBSD measurements to filter out the recrystallized grains and the Dauphiné twins gives the closest stress estimate to the recrystallized grain stress estimates from table 3.

Conclusions

When measuring the average subgrain sizes, the manually applied linear intersect method is still the most accurate option. This is because in many cases a decision has to be made whether to count certain grain boundaries as subgrain boundaries or not.

These decisions are difficult for a computer program to make in a correct manner.

While SEM-CL is a useful and fast method for detecting subgrains, it cannot be used by itself. Because SEM-CL cannot make a distinction between subgrains, recrystallized grains and Dauphiné twins, it always has to be used in combination with a method that can distinguish between these structures, like EBSD.

SEM-CL can be used as a viable way to check if EBSD maps have picked up all the subgrain boundaries in a sample. This is because SEM-CL can detect microstructures that have a lower angular misorientation than EBSD can measure.

When used in combination SEM-CL and EBSD can provide an accurate measurement of even low angle misorientation subgrain boundaries without confusing them with other microstructures like Dauphiné twins.

Acknowledgements

I want to thank my supervisors Prof. dr. Martyn Drury and Dr. Maartje Hamers for their guidance and advice during this project. I also want to thank Dr. Maartje Hamers and Dr. Eric Hellebrand for their assistance with SEM, electron microprobe and EBSD measurements.

References

Brough, I., Bate, P. S., & Humphreys, F. J. (2006). Optimising the angular resolution of EBSD. *Materials Science and Technology*, *22*(11), 1279-1286.

Gleason, G. C., & Tullis, J. (1995). A flow law for dislocation creep of quartz aggregates determined with the molten salt cell. *Tectonophysics*, *247*(1-4), 1-23.

Goddard, R. M., Hansen L., Wallis D., Stipp M., Holyoke, C. III, Kohlstedt D. (T.B.D.). An EBSD-calibrated subgrain-size piezometer. **{T.B.D. is an acronym for "to be decided" as this paper is yet to be published}**

Götze, J. (2009). Chemistry, textures and physical properties of quartz–geological interpretation and technical application. *Mineralogical Magazine*, *73*(4), 645-671.

Götze, J., Plötze, M., Fuchs, H., & Habermann, D. (1999). Defect structure and luminescence behaviour of agate–results of electron paramagnetic resonance (EPR) and cathodoluminescence (CL) studies. *Mineralogical Magazine*, *63*(2), 149-163d.

Götze, J., Plötze, M., & Habermann, D. (2001). Origin, spectral characteristics and practical applications of the cathodoluminescence (CL) of quartz–a review. *Mineralogy and petrology*, *71*(3-4), 225-250.

Hamers, M. F., Pennock, G. M., & Drury, M. R. (2016). Scanning electron microscope cathodoluminescence imaging of subgrain boundaries, twins and planar deformation features in quartz. Physics and Chemistry of Minerals, 44(4), 263-275.

Lloyd, G. E. (2000). Grain boundary contact effects during faulting of quartzite: an SEM/EBSD analysis. *Journal of Structural Geology*, *22*(11-12), 1675-1693.

Neumann, B. (2000). Texture development of recrystallized quartz polycrystals unravelled by orientation and misorientation characteristics. *Journal of Structural Geology*, *22*(11-12), 1695-1711.

Norton, M. G. (1982). The kinematic and microstructural development of some shear zones. *Department of Geology, Royal School of mines. Imperial college of Science and Technology.*

Pickering, F. B. (1976). *The basis of quantitative metallography*(pp. 8-10). London: Metals and Metallurgy Trust for the Institute of Metallurgical Technicians.

Pennock, G. M., Drury, M. R., Trimby, P. W., & Spiers, C. J. (2002). Misorientation distributions in hot deformed NaCl using electron backscattered diffraction. *Journal of microscopy*, *205*(3), 285-294.

Rudnick, R. L., & Gao, S. (2003). Composition of the continental crust. *Treatise on geochemistry*, *3*, 659.

Smith, C. S., & Guttman, L. (1953). Measurement of internal boundaries in three-dimensional structures by random sectioning. *JOM*, *5*(1), 81-87.

Spry, A., Turner, R. G., & Tobin, R. C. (1969). Optical phenomena associated with brazil-twin boundaries in quartz. *American Mineralogist: Journal of Earth and Planetary Materials*, *54*(1-2), 117-133.

Stipp, M., & Tullis, J., (2003). The recrystallized grain size piezometer for quartz. Geophysical research letters, vol. 30, no. 21, 2088.

Trimby, P. W., & Prior, D. J. (1999). Microstructural imaging techniques: a comparison between light and scanning electron microscopy. *Tectonophysics*, *303*(1-4), 71-81.

Twiss, R. J. (1977). Theory and applicability of a recrystallized grain size paleopiezometer. In Stress in the Earth (pp. 227-244). Birkhäuser, Basel.

Wallis, D., Hansen, L. N., Tasaka, M., Kumamoto, K. M., Parsons, A. J., Lloyd, G. E., ... & Wilkinson, A. J. (2019). The impact of water on slip system activity in olivine and the formation of bimodal crystallographic preferred orientations. *Earth and Planetary Science Letters*, *508*, 51-61.

Wedepohl, K. H. (1995). The composition of the continental crust. *Geochimica et cosmochimica Acta*, *59*(7), 1217-1232.

White, S. (1979). Grain and sub-grain size variations across a mylonite zone. *Contributions to Mineralogy and Petrology*, *70*(2), 193-202

Appendix 1a. All images in this appendix were taken from sample CC98-4. a. Light microscope image in XPL. b. SEM-CL red filtered image of the same area as part a of this appendix. The red circle surrounds the same area in both images.

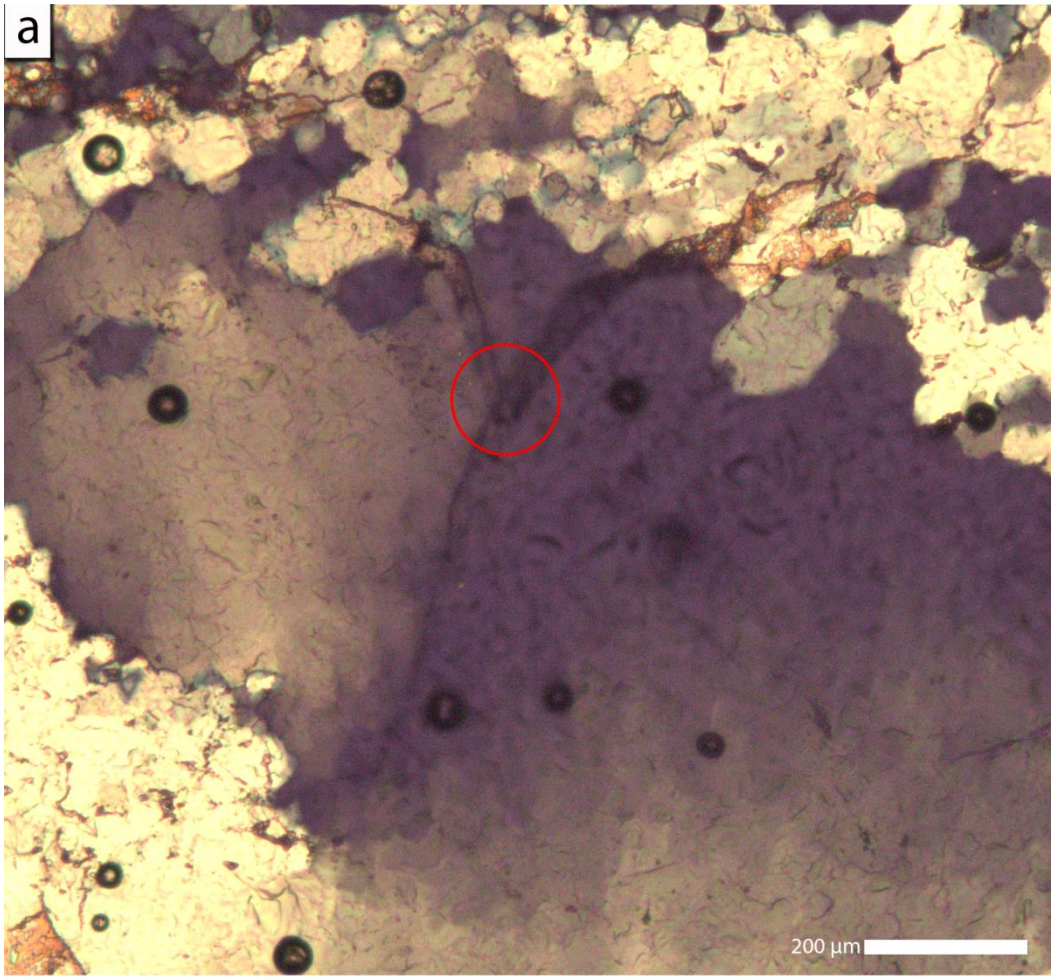

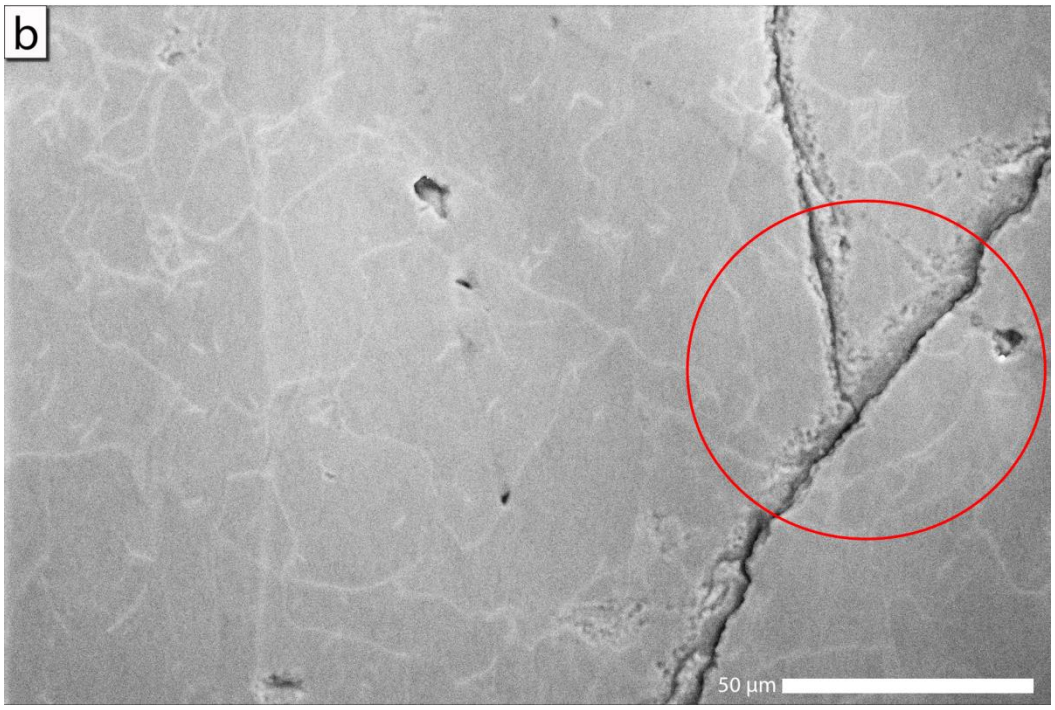

Appendix 1b. All images in this appendix were taken from sample CC98-4c. a. Light microscope image in XPL. b. SEM-CL red filtered image of the same area as part a of this appendix. The red circle surrounds the same area in both images.

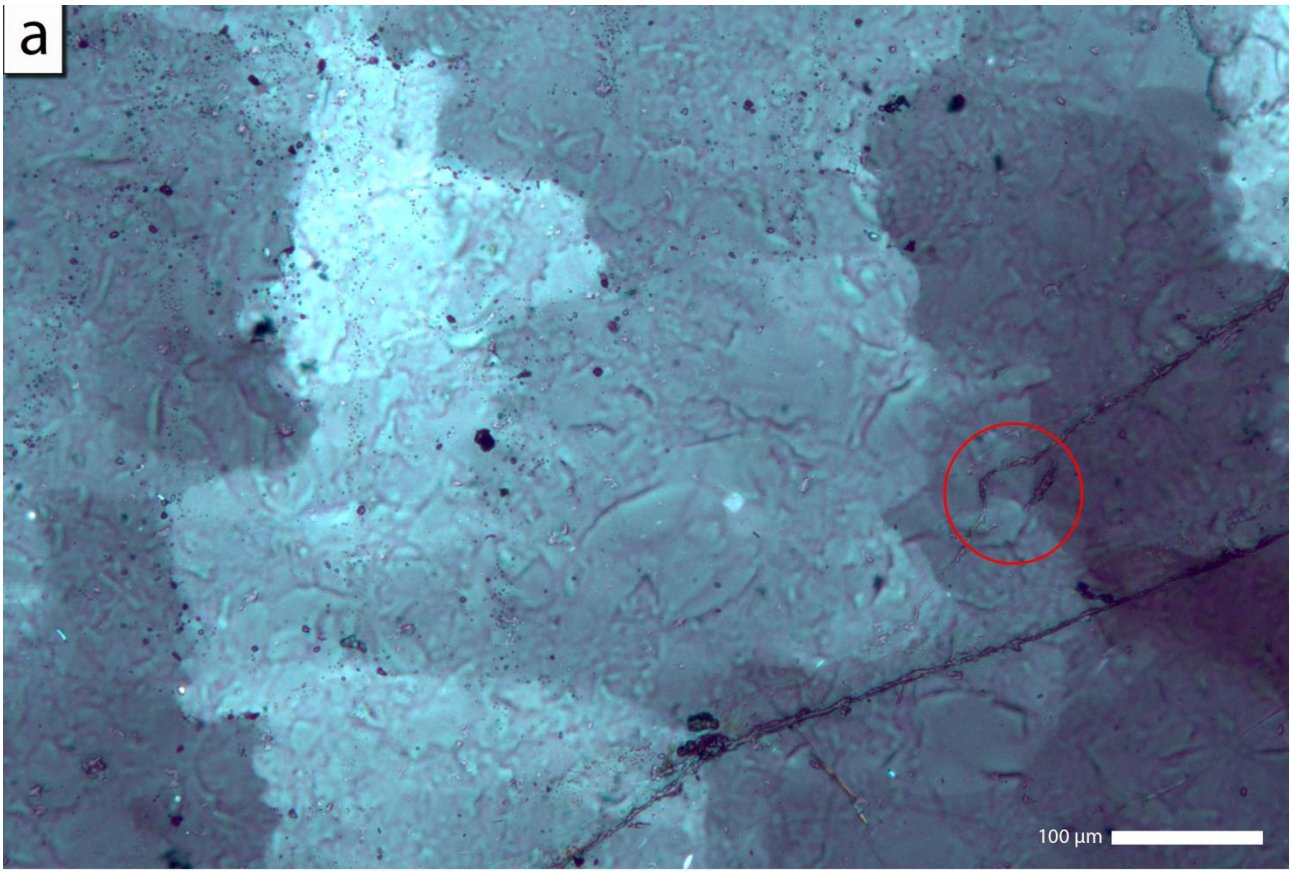

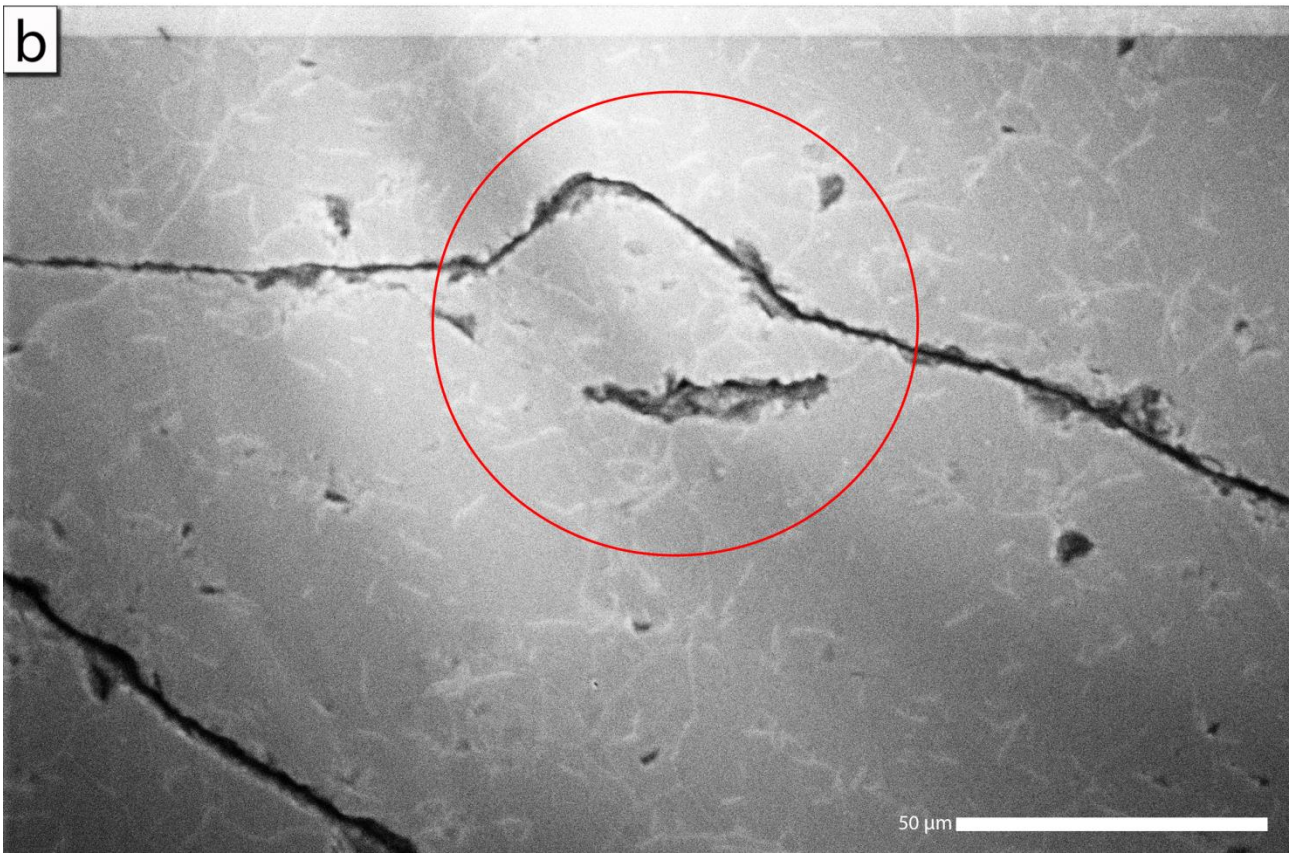

Appendix 1c. All images in this appendix were taken from sample CML-2. a. Light microscope image in XPL. b. SEM-CL red filtered image of the same area as part a of this appendix. The red circle surrounds the same area in both images.

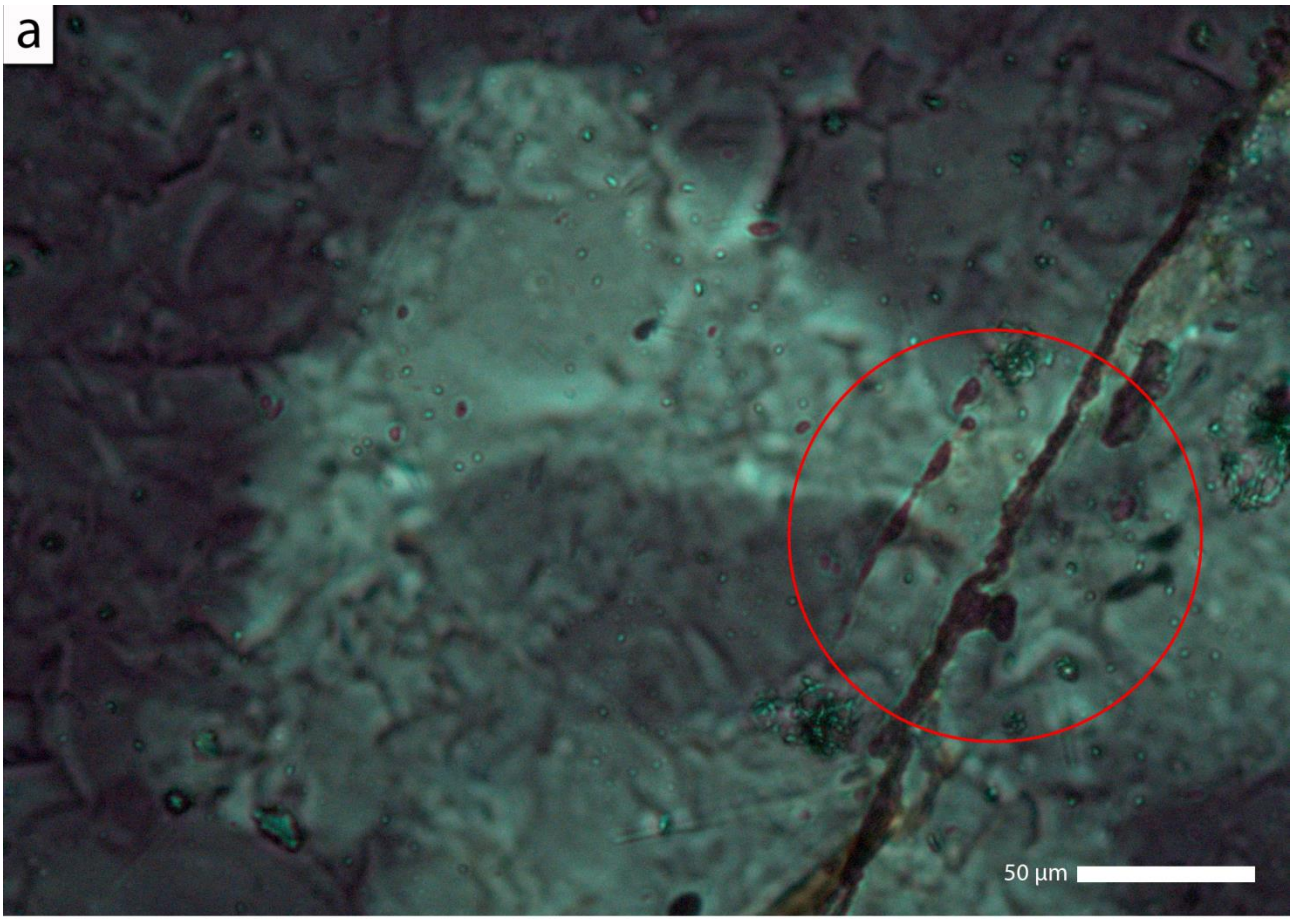

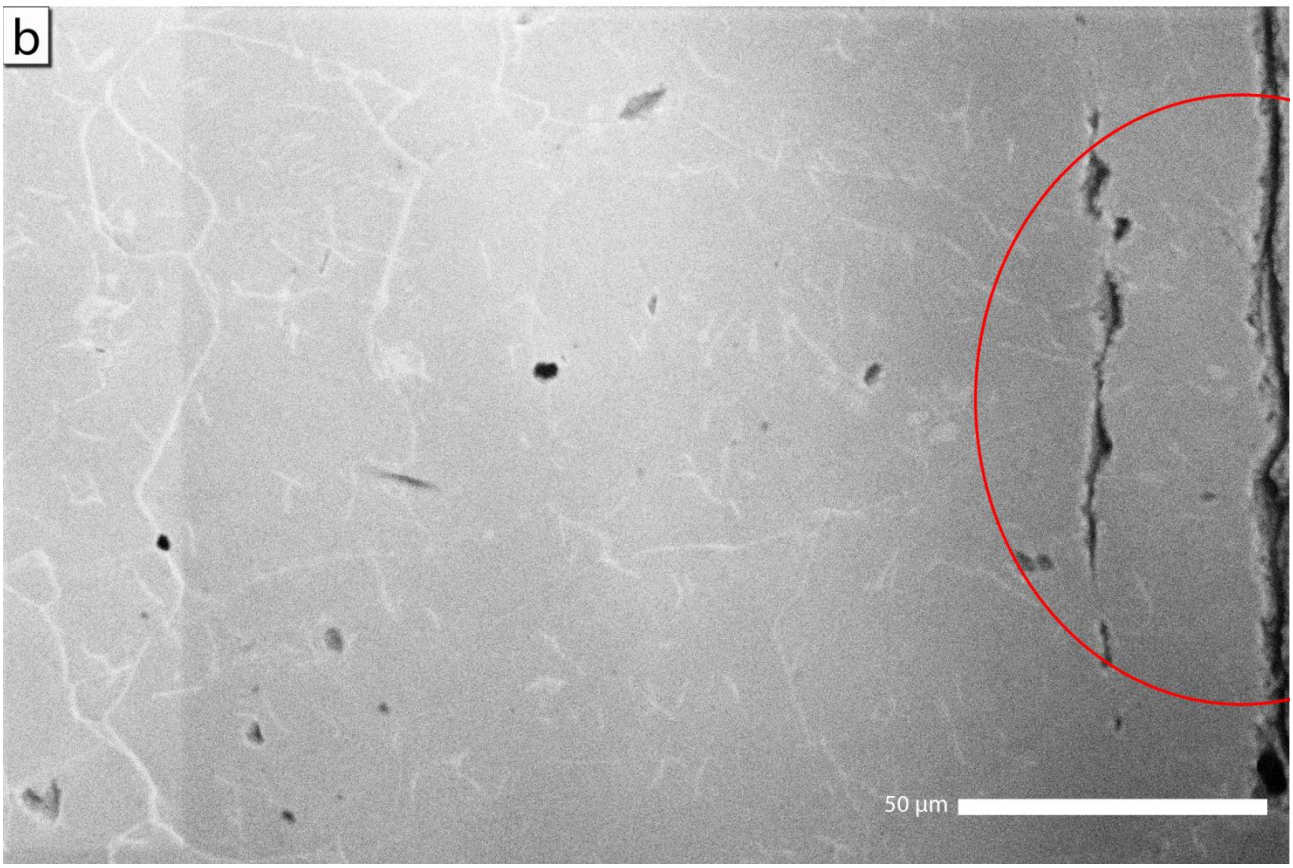

Appendix 1d. All images in this appendix were taken from sample 1024. a. Light microscope image in XPL. b. SEM-CL blue filtered image of the same area as part a of this appendix. The red circles, blue circles and red arrows indicate the same areas in both images.

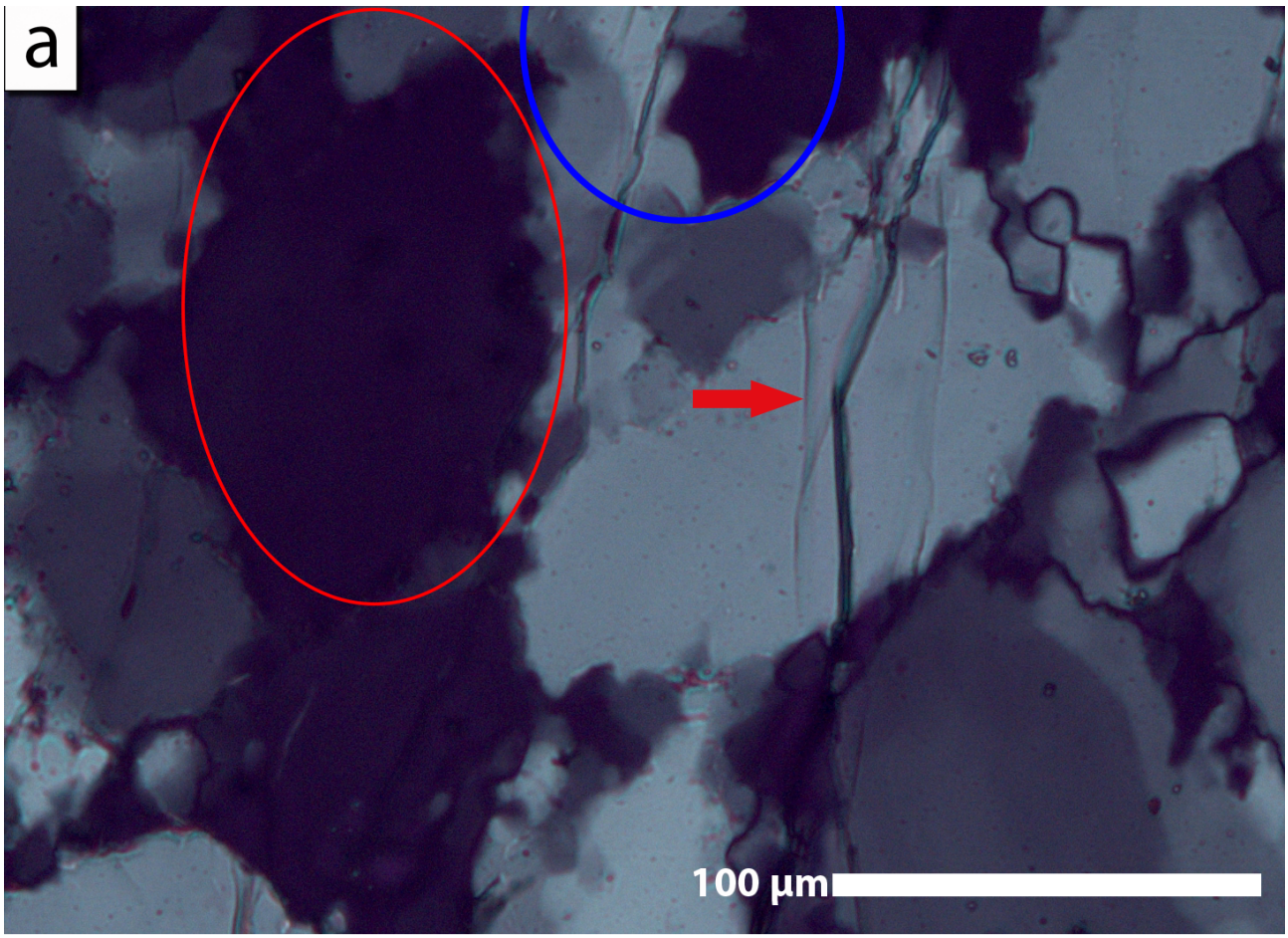

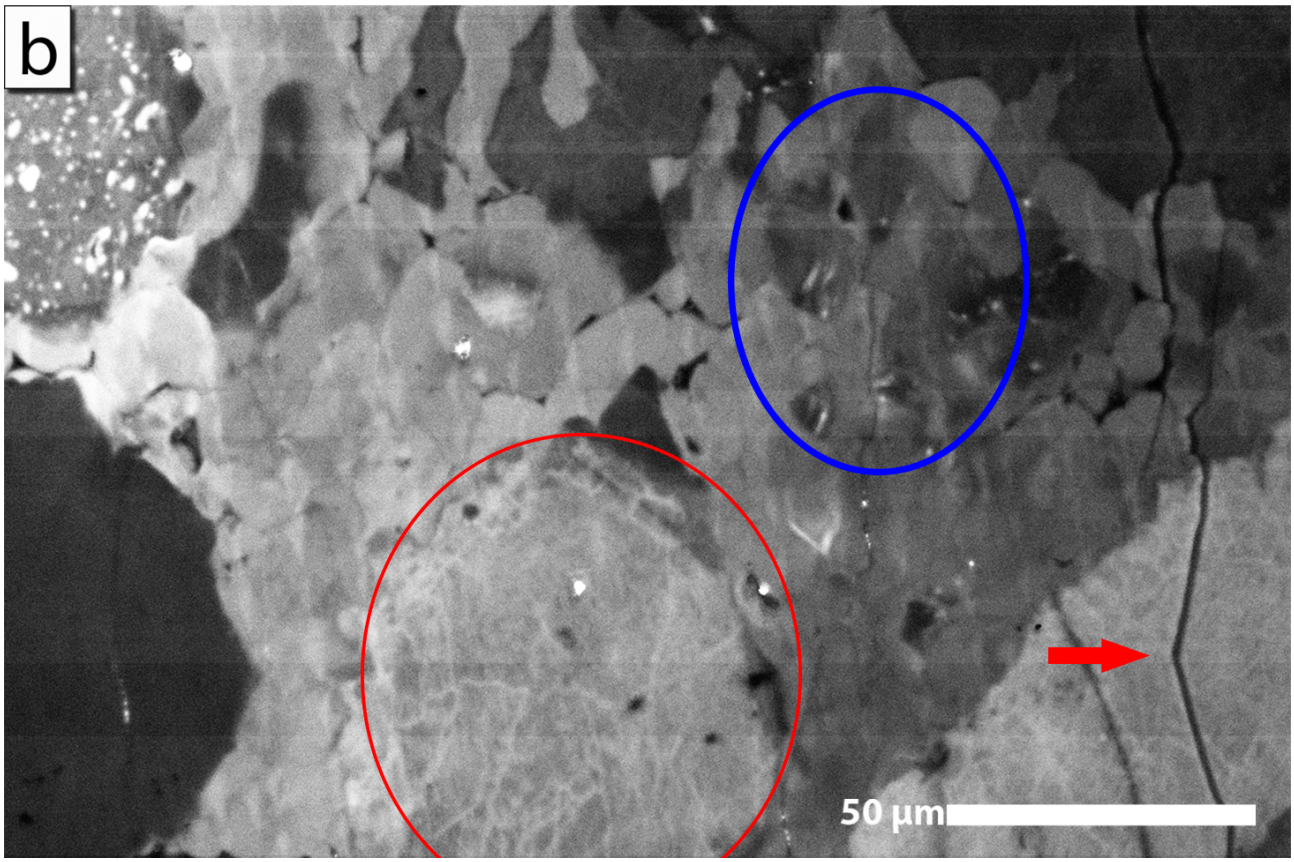

Appendix 2a. SEM-CL red filtered composite image of sample CC98-4

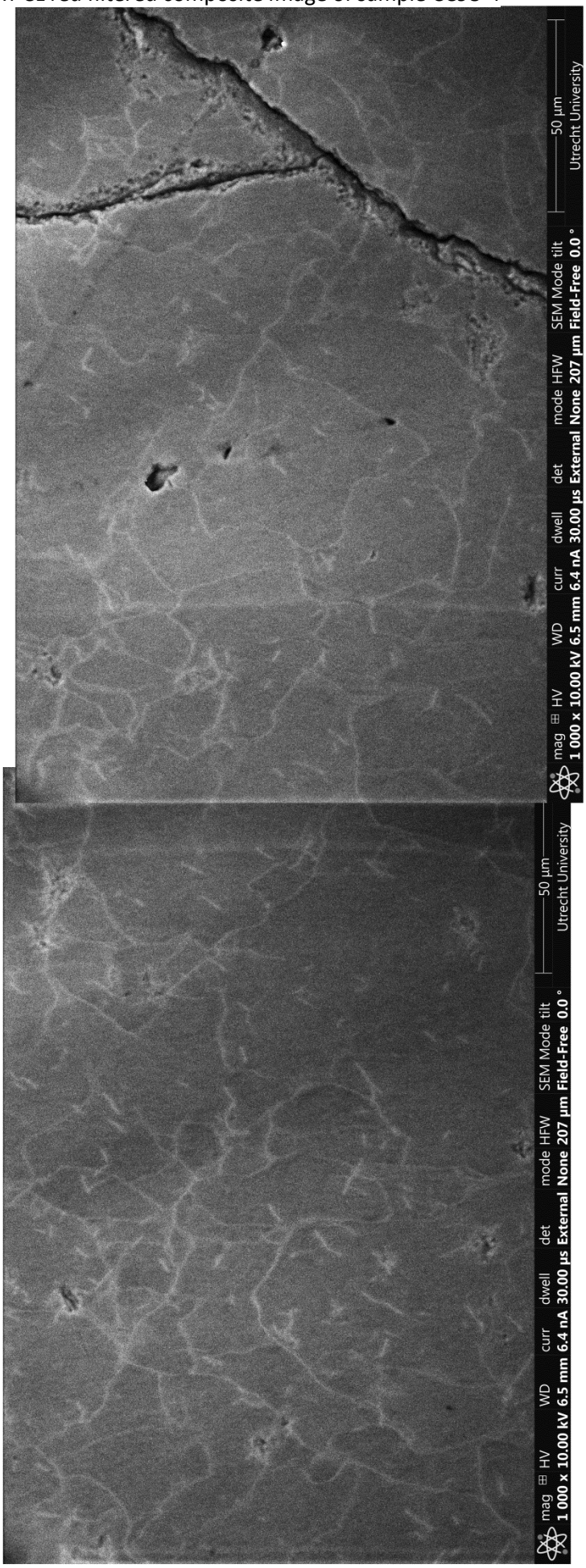

Appendix 2b. SEM-CL red filtered composite image of sample CC98-4c

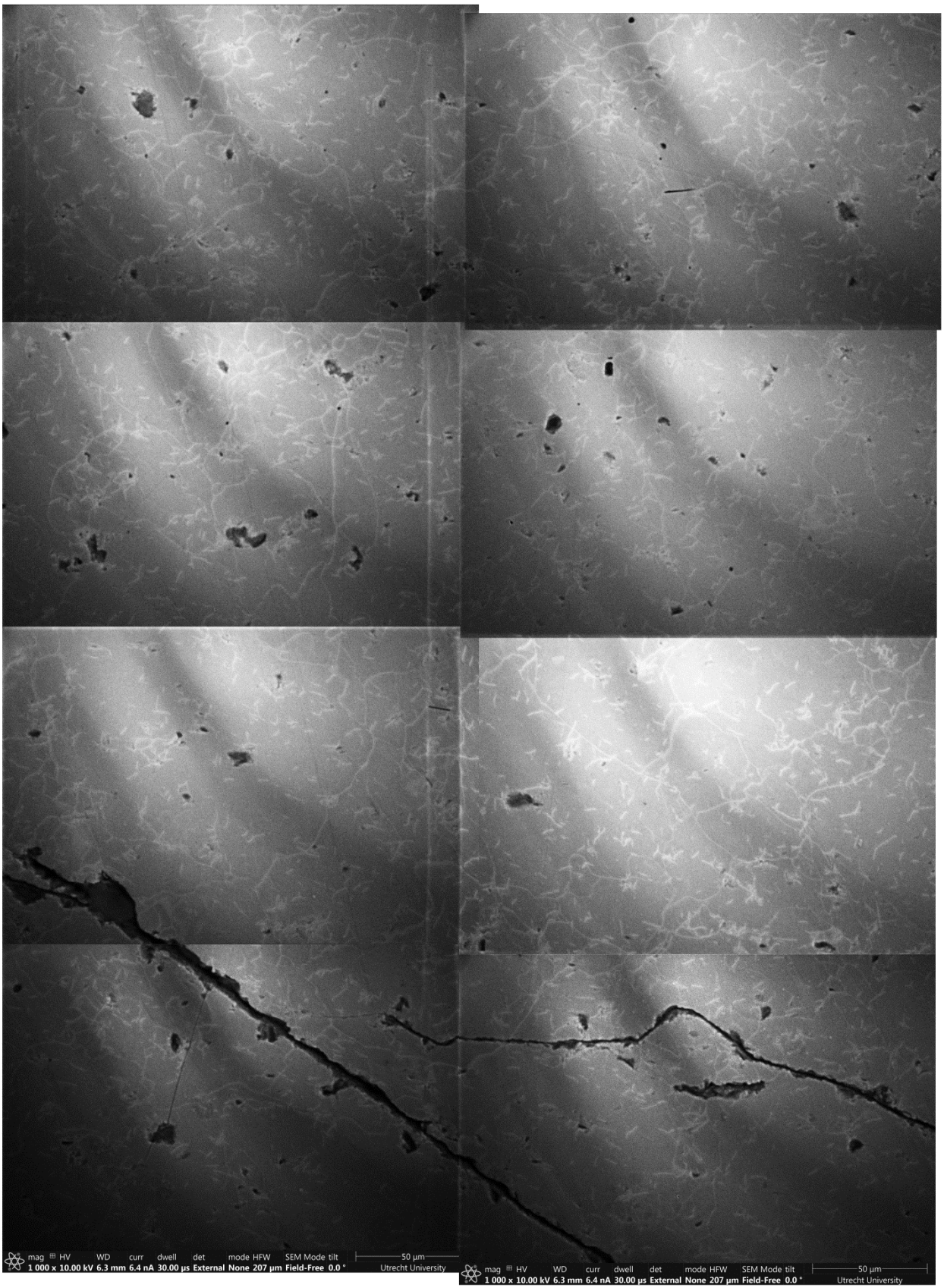

Appendix 2c. SEM-CL red filtered composite image of sample CML-2 *(Red line indicates where the image should be attached)*

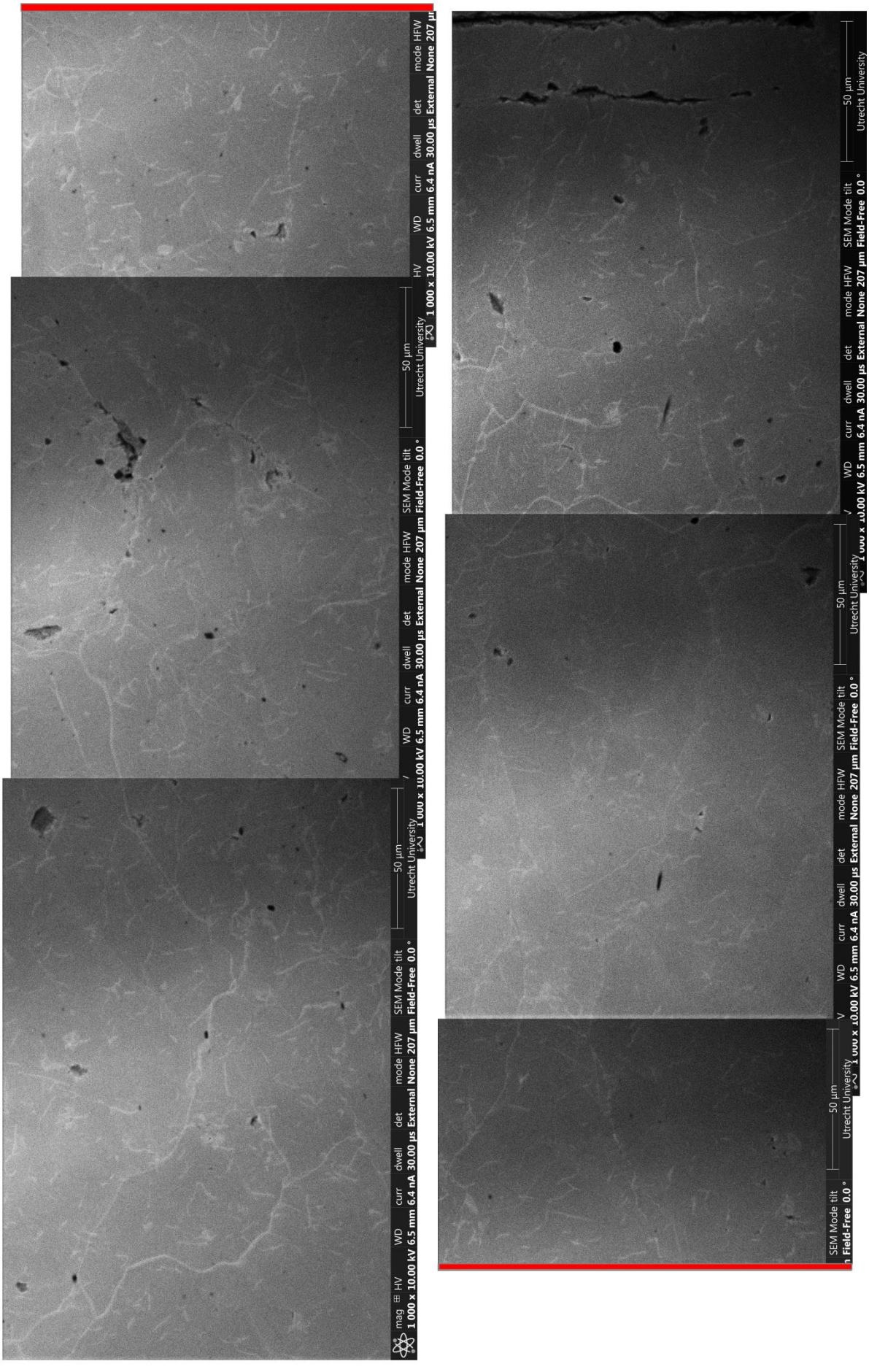

Appendix 2d. SEM-CL red filtered composite image of sample 1024

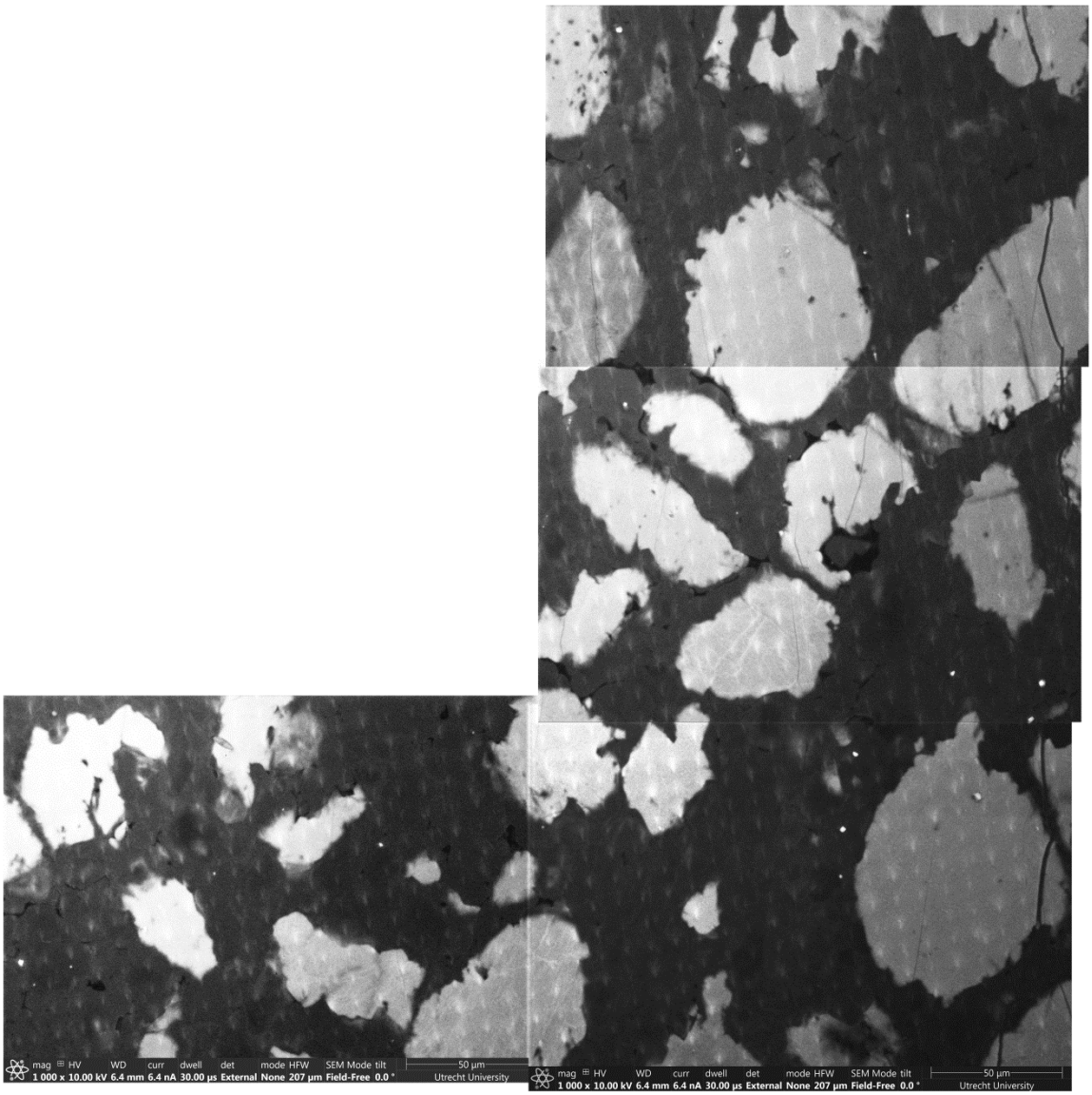

Appendix 2e. SEM-CL blue filtered composite image of sample 1024

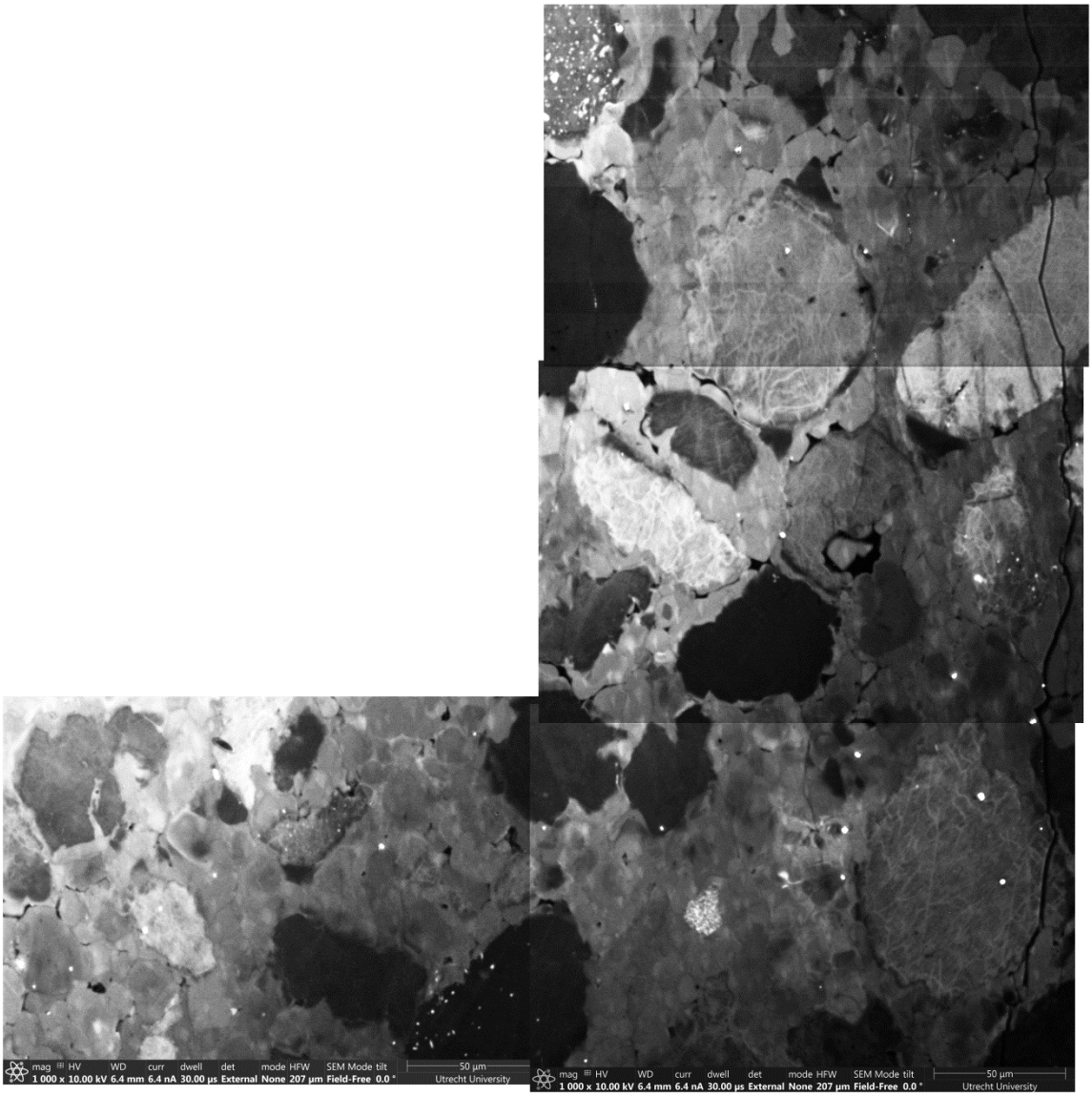

Appendix 2f. SEM-CL RGB composite image of sample 1024

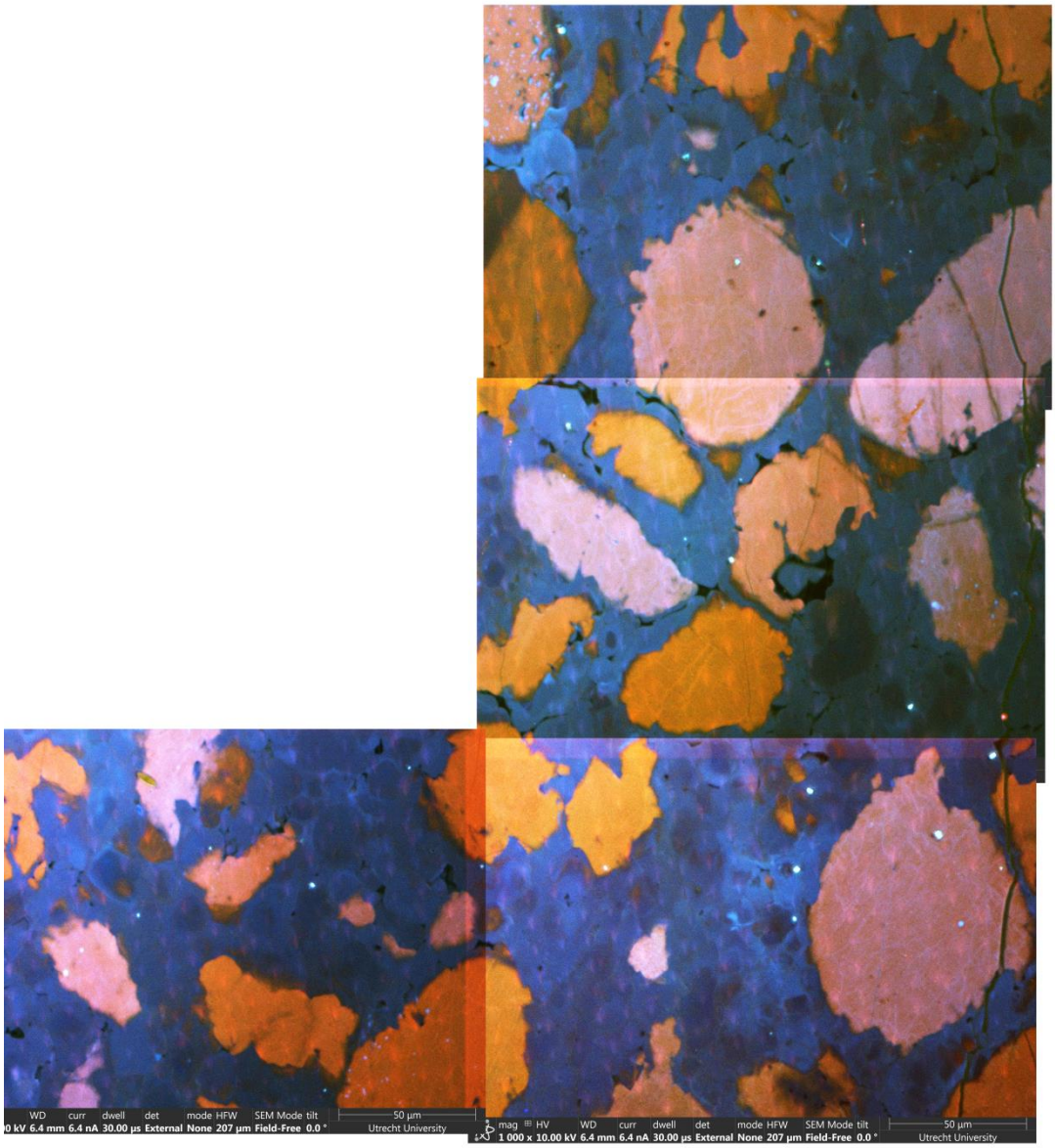

Appendix 3a. All images and maps in this appendix were taken from sample CC98-4. a. Electron microprobe map depicting the emission intensity of the red colour wavelength (~500-850 nm). b. Same microprobe map as part a of this appendix, with manually traced possible subgrain boundaries in red. c. SEM-CL red filtered image depicting the same area as part a of this appendix. d. SEM-CL red filtered image with an overlay of the possible subgrain boundaries depicted in part b of this appendix.

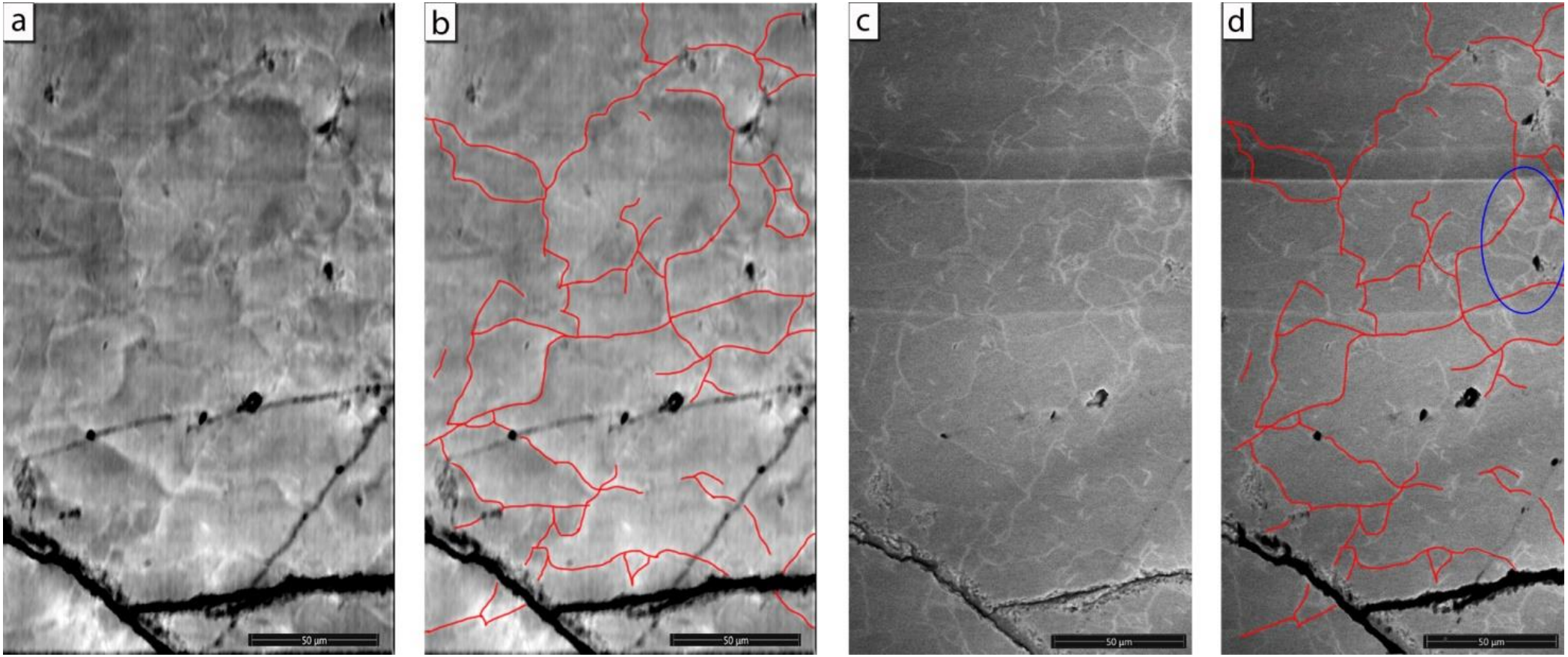

Appendix 3b. All images and maps in this appendix were taken from sample CC98-4c. a. Electron microprobe map depicting the emission intensity of the red colour wavelength (~500-850 nm). b. Same microprobe map as part a of this appendix, with manually traced possible subgrain boundaries in red. c. SEM-CL red filtered image depicting the same area as part a of this appendix. d. SEM-CL red filtered image with an overlay of the possible subgrain boundaries depicted in part b of this appendix.

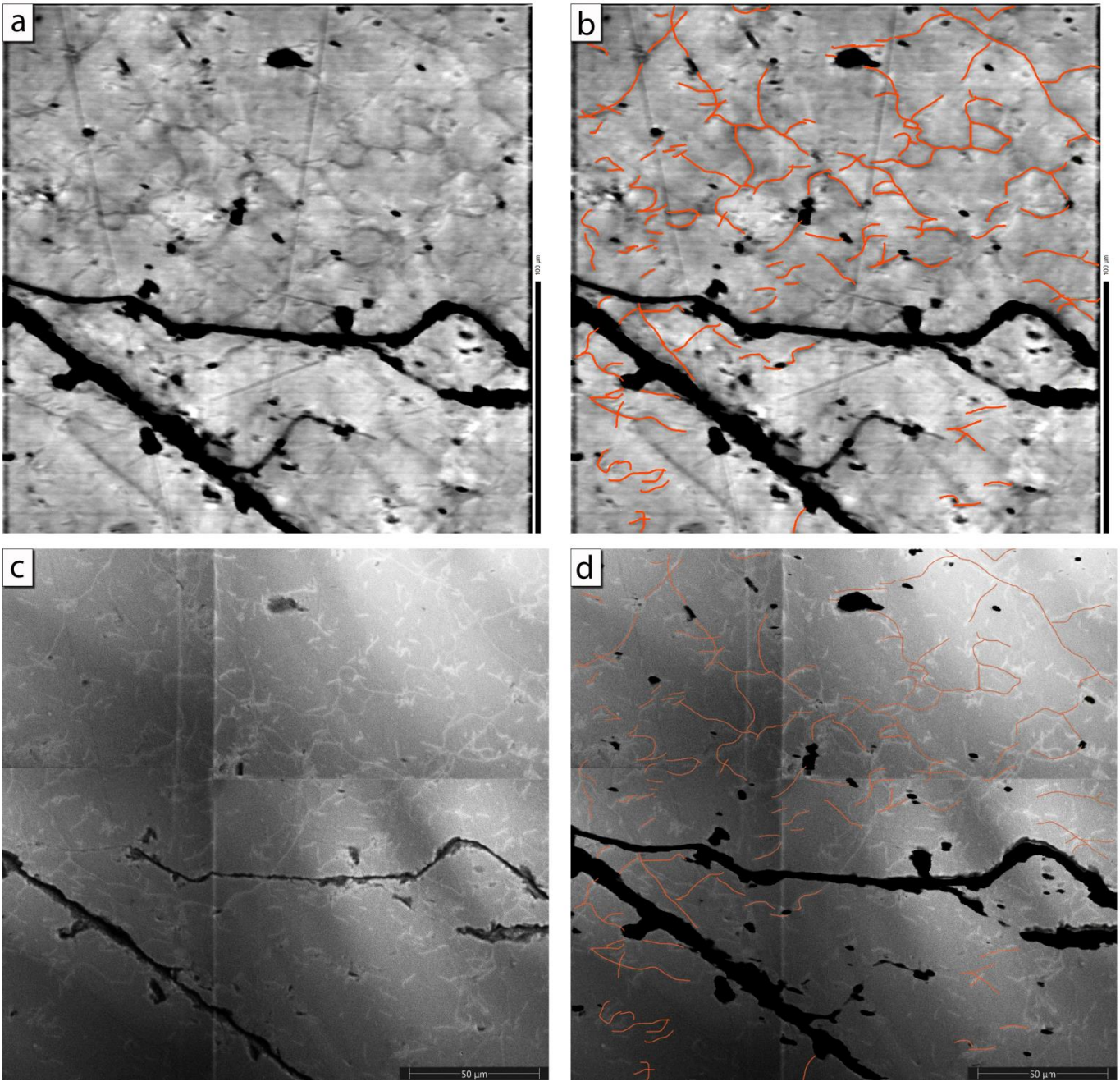

Appendix 3c. All images and maps in this appendix were taken from sample CML-2. a. Electron microprobe map depicting the emission intensity of the red colour wavelength (~500-850 nm). b. Same microprobe map as part a of this appendix, with manually traced possible subgrain boundaries in red. c. SEM-CL red filtered image depicting the same area as part a of this appendix. d. SEM-CL red filtered image with an overlay of the possible subgrain boundaries depicted in part b of this appendix.

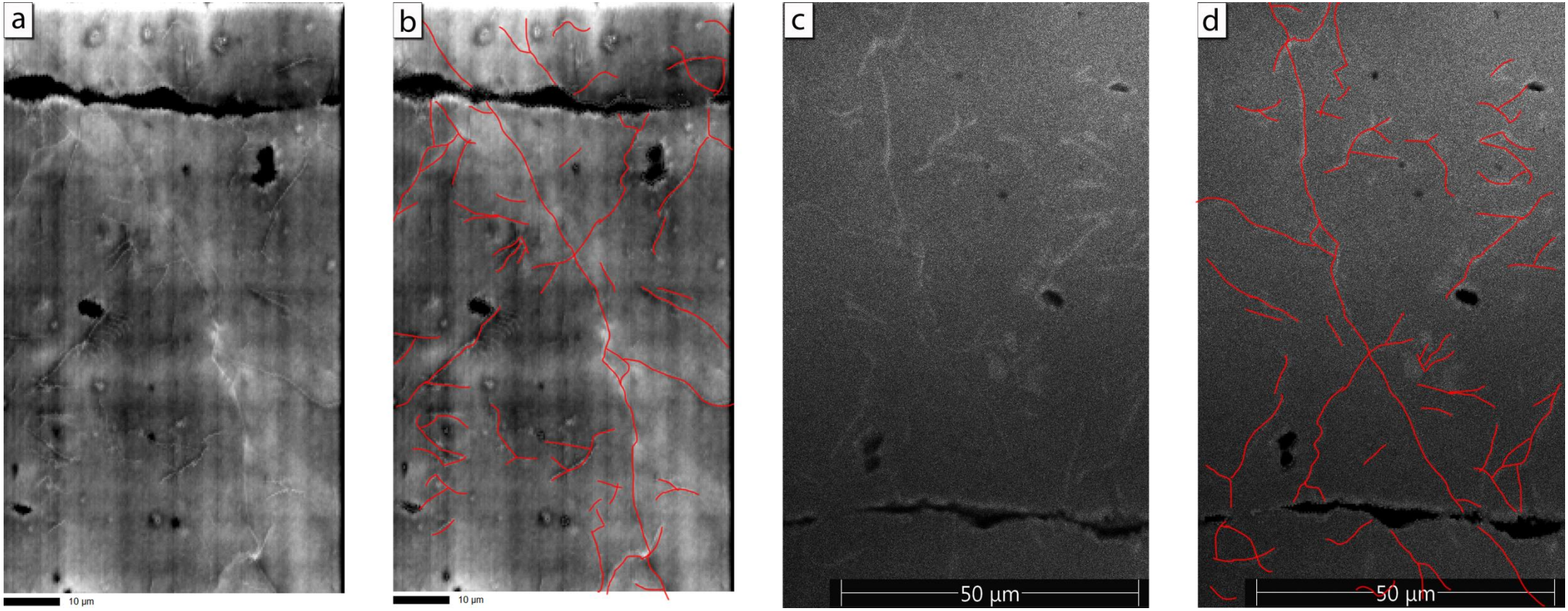

Appendix 3d. All images and maps in this appendix were taken from sample 1024. a. Electron microprobe map depicting the emission intensity of the red colour wavelength (~500-850 nm). b. Same microprobe map as part a of this appendix, with manually traced possible subgrain boundaries in red. c. SEM-CL blue filtered image depicting the same area as part a of this appendix. d. SEM-CL blue filtered image with an overlay of the possible subgrain boundaries depicted in part b of this appendix.